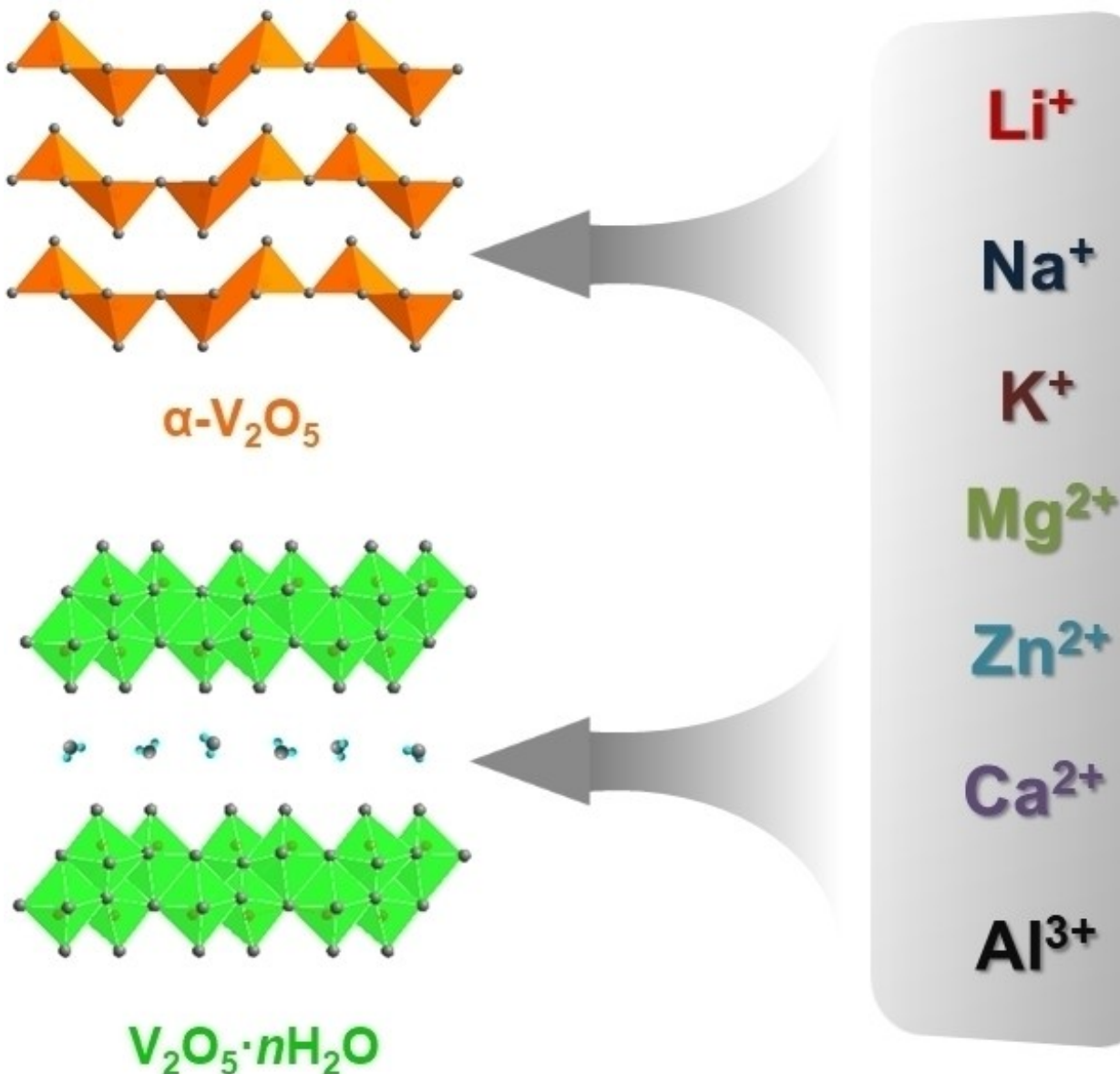


Structure Evolution of V_2O_5 as Electrode Materials for Metal-Ion Batteries

Xiaogang Niu,^[a, b] Nan Li,^[a] Yifan Chen,^[a] Jianwen Zhang,^[a] Yusi Yang,^[a] Lulu Tan,^[a] Jianghao Wu,^[b] Lin Guo,^[a] and Yujie Zhu^{*[a, c]}



With the increasing demand for next-generation electrochemical energy storage systems, various kinds of metal-ion batteries have been developed in the past several decades, such as lithium-ion batteries (LIBs), sodium-ion batteries (NIBs), potassium-ion batteries (KIBs), magnesium-ion batteries (MIBs), zinc-ion batteries (ZIBs), calcium-ion batteries (CIBs), and aluminum-ion batteries (AIBs). Due to its open structure, large interlayer spacings, multiple valence states, and reversible structural variations, layered V_2O_5 , including two polymorphs of single layered α - V_2O_5 and double layered $V_2O_5 \cdot nH_2O$, has been

reported as a universal electrode material for all kinds of metal-ion batteries mentioned above. In this review, we aim to summarize and compare the structure evolution of α - V_2O_5 and $V_2O_5 \cdot nH_2O$ during the insertion/extraction of various kinds of metal-ions. This short review is expected to be helpful to comprehensively understand the structure evolution mechanism of α - V_2O_5 and $V_2O_5 \cdot nH_2O$ reacting with different metallic charge carriers and inspire the development of new electrode materials for high-performance metal-ion batteries.

1. Introduction

With the rapid increase of world population and technological advances, environmental degradation and energy crisis are becoming major challenges for human society. Replacing non-renewable fossil fuels with environmentally benign and renewable energy, such as solar, wind, wave, etc., has been accelerated in recent decades.^[1–3] However, these renewable energy sources cannot be used directly as their intermittent characteristics. Therefore, grid-level energy storage systems are required to store them before they can be supplied to fit different application scenarios. Among all grid-level energy storage solutions, for example compressed air storage, pumped water storage, and flywheel energy storage, metal-ion batteries with high energy density, high efficiency, and long lifespan have been regarded as one of the most promising candidates. Among them, lithium-ion batteries (LIBs) have been successfully commercialized in energy storage market and applied in portable equipment and electric vehicles.^[4] Nevertheless, the limited lithium reserves and the boosting lithium precursor price hinder the suitability of LIBs for grid-level energy storage. Over the past decades, "beyond Li-ion" batteries, such as sodium-ion batteries (NIBs),^[5–8] potassium-ion batteries (KIBs),^[9–15] magnesium-ion batteries (MIBs),^[16,17] zinc-ion batteries (ZIBs),^[18–22] calcium-ion batteries (CIBs),^[23,24] and aluminum-ion batteries (AIBs),^[25–27] have received considerable attention. As demonstrated in Table 1, alkali metal-ions (Li^+ , Na^+ , and K^+) possess similar properties, endowing that NIBs and KIBs also share similar "rocking-chair" operation mechanism with LIBs. Nevertheless, the accommodation of sodium and potassium-ions for electrode materials is difficult due to their large ionic sizes.^[28] Multivalent metal-ion batteries (MIBs, ZIBs, CIBs, and

AIBs) may have high specific capacities because more than one charge can be provided by Mg^{2+} , Zn^{2+} , Ca^{2+} , and Al^{3+} . Although Mg^{2+} , Zn^{2+} , and Al^{3+} possess similar size with Li^+ , the transport of multivalent metal-ions across the electrolyte/electrode interface/interphase and inside the electrode materials is much more difficult because of the strong electrostatic interaction between multivalent metal-ions and the host materials.^[29] As a consequence, electrode materials with reasonable structure are required to accommodate ions with different sizes and valence states.

Up to now, various kinds of electrode materials with diverse crystal structures have been reported for metal-ion batteries, including one-dimensional (1D) tunnel structure,^[30–35] two-dimensional (2D) layered structure,^[36–41] three-dimensional (3D) framework structure,^[42–48] and rock salt structure.^[49–51] Over the past decades, 2D layered materials have been widely studied.^[52–54] In 1976, the concept of intercalation electrodes was first reported by Whittingham based on layered TiS_2 .^[55] In 1991, the first commercialized LIB created by Sony Corporation was comprised of layered $LiCoO_2$ cathode and carbonaceous anode.^[56] Layered materials are characterized by their large interlayer spacings and wide 2D ion transport paths, allowing them to accommodate a variety of metallic and nonmetallic charge carriers.^[57]

Among all reported layered materials, V_2O_5 , which includes two polymorphs of single layered α - V_2O_5 and double layered $V_2O_5 \cdot nH_2O$, displays intriguing features such as flexible interlayer spacing, abundant redox-active sites, multiple oxidation states ranging from +2 to +5, etc., making it an attractive and universal electrode material for various metal-ion batteries including LIBs, NIBs, KIBs, MIBs, ZIBs, CIBs, and AIBs.^[11,58–67] For example, V_2O_5 displays a specific capacity of ~ 442 mAh g⁻¹ in LIBs corresponding to 3 eq. lithium embedded per V_2O_5 formula unit, which is much higher than that of $LiCoO_2$ (~ 137 mAh g⁻¹, 0.5 equiv. lithium per formula unit).^[68]

Because charge carriers, Li^+ , Na^+ , K^+ , Mg^{2+} , Zn^{2+} , Ca^{2+} , and Al^{3+} , have different sizes and valence states, the structure evolution of α - V_2O_5 and $V_2O_5 \cdot nH_2O$ in these metal-ion batteries is highly ion-dependent. It is necessary to summarize and compare the structure evolution of α - V_2O_5 and $V_2O_5 \cdot nH_2O$ during the ion insertion-extraction process. In 2016, the applications of $V_2O_5 \cdot nH_2O$ as electrode materials for LIBs, NIBs, and MIBs were reviewed by Passerini et al.^[60] In 2020, Mai et al.^[62] made a comprehensive overview of vanadium-based compounds including V_2O_5 , VO_2 , etc., as electrode materials for

[a] Dr. X. Niu, N. Li, Y. Chen, J. Zhang, Y. Yang, Dr. L. Tan, Prof. L. Guo, Prof. Y. Zhu

School of Chemistry
Beihang University
Beijing 100191 (P. R. China)
E-mail: yujiezhu@buaa.edu.cn

[b] Dr. X. Niu, Prof. J. Wu
School of Transportation Science and Engineering
Beihang University
Beijing 100191 (P. R. China)

[c] Prof. Y. Zhu
Beijing Advanced Innovation Center for Biomedical Engineering
Beihang University
Beijing 100191 (P. R. China)

Table 1. Comparison of physicochemical properties for various metal anodes.

	Li ⁺	Na ⁺	K ⁺	Mg ²⁺	Ca ²⁺	Zn ²⁺	Al ³⁺
Ionic radius [Å]	0.76	1.02	1.37	0.66	1.06	0.74	0.56
Standard reduction potential [V vs. SHE]	-3.04	-2.71	-2.93	-2.37	-2.87	-0.76	-1.66
Relative atomic mass	6.94	22.99	39.10	24.31	40.08	65.41	26.98
Volumetric capacity [mAh cm ⁻³]	2062	1128	591	3833	2073	2073	8046
Specific capacity [mAh g ⁻¹]	3861	1166	685	2205	1337	820	2980

metal-ion batteries beyond LIBs. More recently, Fan et al.^[69] reviewed the development of vanadium-based materials for aqueous metal-ion batteries, with the emphasis on ZIBs. These

existing reviews focus more on the electrochemical performance of materials while the structure evolution of α -V₂O₅ and



Xiaogang Niu received his Ph.D. in materials physics and chemistry from Beihang University in 2022. He is currently working as a postdoctoral fellow at Beihang University. His current research interests focus on electrode materials and electrolyte for high-performance metal-ion batteries.



Lulu Tan received her Ph.D. degree in chemistry from the Beihang University in 2022. Now, she is a postdoctoral fellow at the school of physics in Beihang University. Her research interests mainly focus on material design and electrochemical mechanism investigation for K-ion batteries.



Nan Li received his Master of Science degree material science from the East China University of Science and Technology in 2021. He is now a Ph.D. candidate under the guidance of Prof. Yujie Zhu at Beihang University. His current research interests focus on K-ion batteries.



Jianghao Wu is a professor at the School of Transportation Science and Engineering in Beihang University. He received his Ph.D. in fluid mechanics from Beihang University in 2004. In the same year, he joined the postdoctoral research Station of Aerospace Science and Technology. In 2006, he taught at the Flight Mechanics Department of School of Aviation Science and Engineering in Beihang University. He is mainly engaged in the research of bionic fluid.



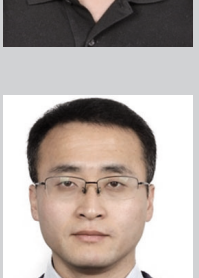
Yifan Chen received his Master of Science degree (chemistry) in 2023 from Beihang University in China under the supervision of Prof. Yujie Zhu. Currently, he is a Ph.D. candidate in Inorganic Chemistry at Beihang University. His research mainly focuses on investigating reaction mechanism of electrode materials for Li-ion and K-ion batteries.



Lin Guo is a full professor in the School of Chemistry, Beihang University. He received his Ph.D. degree from the Beijing University of Institute of Technology in 1997. He was a visiting scholar at the Hong Kong University of Science and Technology in 1999 and worked for 2 years at Dresden University of Technology. His research interests focus on developing new synthetic methods for nanomaterials and exploring the nature of their potential applications.



Jianwen Zhang graduated from Central South University in 2019 with a master's degree in chemical engineering and technology. He is presently a Ph.D. student at Beihang University, where he works with Prof. Yujie Zhu. His study focuses on electrolytes for anode-free alkali metal batteries.



Yujie Zhu is a full professor in the School of Chemistry, Beihang University. He received his bachelor and Ph.D. degree from Tsinghua University in 2006 and University of Maryland College Park (supervisor: Prof. Chunsheng Wang) in 2013. After two years training as a postdoc in Prof. Chunsheng Wang's group, he joined in Beihang University in 2016. His research interests focus on developing electrode materials and electrolytes for metal-ion batteries.



Yusi Yang is currently a Ph.D. candidate under the guidance of Prof. Yujie Zhu in the school of chemistry, Beihang University. His research interests lie in developing novel low-temperature electrolytes for alkali metal-ion batteries.

$\text{V}_2\text{O}_5 \cdot n\text{H}_2\text{O}$ in different metal-ion (Li^+ , Na^+ , K^+ , Mg^{2+} , Zn^{2+} , Ca^{2+} , and Al^{3+}) batteries are not given in detail.

In this review, we aim to systematically summarize and compare the structure evolution of $\alpha\text{-V}_2\text{O}_5$ and $\text{V}_2\text{O}_5 \cdot n\text{H}_2\text{O}$ during insertion and extraction of different metal-ions including Li^+ , Na^+ , K^+ , Mg^{2+} , Zn^{2+} , Ca^{2+} , and Al^{3+} . The structure of this review is organized as follows: first, the detailed crystal structures of $\alpha\text{-V}_2\text{O}_5$ and $\text{V}_2\text{O}_5 \cdot n\text{H}_2\text{O}$ are introduced in Section 2; then, the structure evolution of $\alpha\text{-V}_2\text{O}_5$ and $\text{V}_2\text{O}_5 \cdot n\text{H}_2\text{O}$ as electrode materials for LIBs, NIBs, KIBs, MIBs, ZIBs, CIBs, and AlIBs are systematically presented and discussed in Section 3 and Section 4, respectively; finally, a summary and outlook regarding the future research of $\alpha\text{-V}_2\text{O}_5$ and $\text{V}_2\text{O}_5 \cdot n\text{H}_2\text{O}$ is presented.

2. Crystal Structure of $\alpha\text{-V}_2\text{O}_5$ and $\text{V}_2\text{O}_5 \cdot n\text{H}_2\text{O}$

$\alpha\text{-V}_2\text{O}_5$ belongs to orthorhombic crystal system with space group $Pmmn$ and lattice parameters of $a = 11.510 \text{ \AA}$, $b = 3.559 \text{ \AA}$, $c = 4.371 \text{ \AA}$. As shown in Figure 1(a), $\alpha\text{-V}_2\text{O}_5$ has a layered structure in which edge- and corner-shared $[\text{VO}_5]$ polyhedrons act as the fundamental building block to constitute the single layers.^[70] The poles of $[\text{VO}_5]$ are arranged in the period of up (\uparrow)-up (\uparrow)-down (\downarrow)-down (\downarrow) along the a -direction to form the zigzag $[\text{V}_2\text{O}_5]$ slabs. The adjacent $[\text{V}_2\text{O}_5]$ slabs have an interlayer spacing of $\sim 4.4 \text{ \AA}$ and are stacked by weak van der Waals interaction along the c -direction.^[71] Depending on the difference of coordination environment, O can be classified into apical oxygen (O1), bridging oxygen (O2), and chaining oxygen (O3) (Figures 1a and b). The single apical oxygen (O1) locates in the vanadyl with a V–O length of $\sim 1.54 \text{ \AA}$. Bridging oxygen (O2) connects adjacent $[\text{VO}_5]$ by

corner-sharing with a V–O length of $\sim 1.77 \text{ \AA}$. Chaining oxygen (O3) connects adjacent $[\text{VO}_5]$ by edge-sharing with V–O bond lengths of ~ 1.88 , ~ 1.88 , and $\sim 2.02 \text{ \AA}$. Alternatively, $\alpha\text{-V}_2\text{O}_5$ could be described as the connection of distorted $[\text{VO}_6]$ octahedron, which is formed by one $[\text{VO}_5]$ and another apical oxygen (O1) in the bottom layer with a large V...O distance of $\sim 2.81 \text{ \AA}$ (Figure 1c).

Hydrate $\text{V}_2\text{O}_5 \cdot n\text{H}_2\text{O}$, which belongs to monoclinic crystal system with space group $C2/m$, usually exists in the form of V_2O_5 xerogels and aerogels.^[72] As shown in Figure 2, $\text{V}_2\text{O}_5 \cdot n\text{H}_2\text{O}$ consists of stacked $[\text{V}_2\text{O}_5]$ double layers, which can be considered as the deformed $\alpha\text{-V}_2\text{O}_5$, with H_2O molecules located between the layers. The double layered slabs of $\text{V}_2\text{O}_5 \cdot n\text{H}_2\text{O}$ are formed by arranging two adjacent single V–O layers of $\alpha\text{-V}_2\text{O}_5$; the vanadyl bonds (V–O1) of two adjacent $[\text{V}_2\text{O}_5]$ slabs rotate into the opposite direction forming the bilayer sheet.^[73,74] The distance between two single layers facing away in one bilayered sheet is $\sim 2.9 \text{ \AA}$ (Figure 2b). The double layered sheets can also be regarded as edges-sharing double chains which are formed by $[\text{VO}_6]$ octahedrons. Water molecules are located between the adjacent bilayers, which play a crucial role for stabilizing the double layered structure.^[75] The interlayer spacing of $\text{V}_2\text{O}_5 \cdot n\text{H}_2\text{O}$ is highly dependent on the number of water n in the formula unit. Taking $\text{V}_2\text{O}_5 \cdot \text{H}_2\text{O}$ as an example, it has an interlayer spacing of $\sim 11.5 \text{ \AA}$. It should be noted that $\text{V}_2\text{O}_5 \cdot n\text{H}_2\text{O}$ could reversibly transform into $\alpha\text{-V}_2\text{O}_5$ when the water molecules are completely removed.^[76]

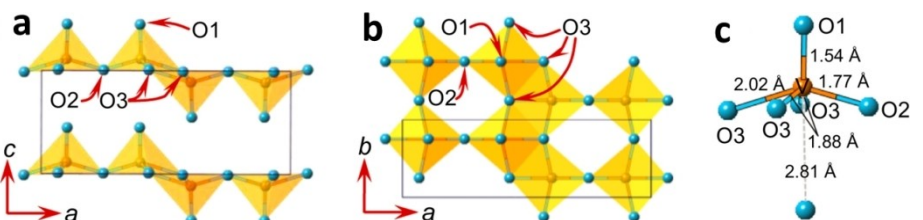


Figure 1. Crystal structure of $\alpha\text{-V}_2\text{O}_5$: Views from a) ac plane and b) ab plane. c) The coordination environment around a single V atom. Reproduced with permission from Ref [70]. Copyright (2017) Elsevier B.V.

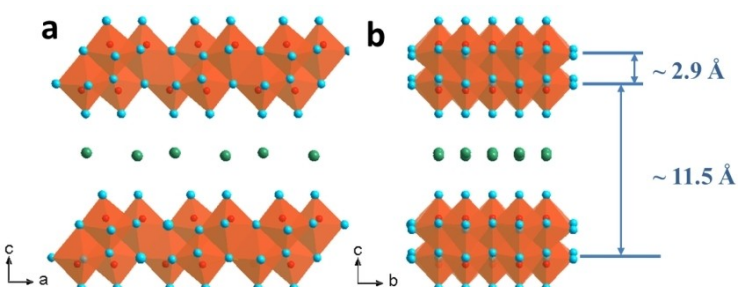


Figure 2. Crystal structure of $\text{V}_2\text{O}_5 \cdot n\text{H}_2\text{O}$: Views from a) ac plane and b) bc plane. Blue and red balls stand for lattice oxygen and vanadium, respectively. For concision, water molecules are shown in green. The polyhedral model is revealed based on $\text{V}_2\text{O}_5 \cdot \text{H}_2\text{O}$ (ICSD #94905) provided by Inorganic Crystal Structure Database (ICSD). CD-ROM, version 2004.

3. Structure Evolution of $\alpha\text{-V}_2\text{O}_5$ in Various Metal-Ion Batteries

3.1. Lithium-ion batteries

In 1976, Whittingham et al.^[55] first reported the electrochemical lithiation of $\alpha\text{-V}_2\text{O}_5$ at room temperature. After that, the structure evolution of $\alpha\text{-V}_2\text{O}_5$ during lithium insertion/extraction was investigated by many studies.^[77–80] The charge-discharge profiles of V_2O_5 during lithium insertion/extraction are shown in Figure 3(a). There are four voltage platforms at ~ 3.2 , ~ 3.1 , ~ 2.1 , and ~ 1.8 V (vs. Li^+/Li) in the first discharge (lithiation) process, which are attributed to four consecutive two-phase reactions, namely $\alpha\text{-}\epsilon$, $\epsilon\text{-}\delta$, $\delta\text{-}\gamma$, and $\gamma\text{-}\omega$.^[81–83] These phase transitions of $\alpha\text{-V}_2\text{O}_5$ are accompanied by the puckering of the $[\text{V}_2\text{O}_5]$ layers (Figure 3b).^[84]

The lithiation products $\text{Li}_x\text{V}_2\text{O}_5$ ($0 < x < 3$) and their crystaline structures are schematically shown in Figure 3(b).^[85] During the initial lithium insertion process ($x < 0.35$), the structure of $\alpha\text{-V}_2\text{O}_5$ is barely changed and the interlayer spacing is slightly expanded. Subsequently, the V_2O_5 host is slightly puckering and $\epsilon\text{-Li}_x\text{V}_2\text{O}_5$ ($0.35 < x < 0.7$) with space group $Pmmn$ is formed.^[86] Due to the electrostatic interaction between lithium atoms and the oxygen atoms, the apical vanadyl (V=O) of $[\text{VO}_5]$ square

polyhedrons skews toward lithium atoms. With the further insertion of lithium, $\delta\text{-Li}_x\text{V}_2\text{O}_5$ ($0.7 \leq x \leq 1$) is formed, which has orthorhombic structure with space group $Amma$. In this structure, the $[\text{V}_2\text{O}_5]$ layers are highly puckered and alternatively shift along the [010] direction by $b/2$ (1/2 length of the unit cell).^[87] It should be noted that α -, ϵ -, and $\delta\text{-Li}_x\text{V}_2\text{O}_5$ have similar layered structure with $[\text{VO}_5]$ period of up (\uparrow)-up (\uparrow)-down (\downarrow)-down (\downarrow) and the phase transitions of $\alpha\text{-}\epsilon$ and $\epsilon\text{-}\delta$ are reversible. The coordination number of lithium is 6 in these structures and the voltage plateaus corresponding to the transition of these phases occur above 3.0 V (vs. Li^+/Li).

However, at a higher lithium insertion content, $\gamma\text{-Li}_x\text{V}_2\text{O}_5$ ($1 < x < 2$) with space group $Pnma$ ($a = 9.70 \text{ \AA}$, $b = 3.61 \text{ \AA}$, $c = 10.66 \text{ \AA}$) will be formed at a voltage plateau at 2.1 V (vs. Li^+/Li). This $\gamma\text{-Li}_x\text{V}_2\text{O}_5$ ($1 < x < 2$) has obvious different puckering arrangement compared with $\delta\text{-Li}_x\text{V}_2\text{O}_5$. Specifically, coupled edge-sharing $[\text{VO}_5]$ pyramids rotate in the opposite direction. The $[\text{VO}_5]$ period turns into up (\uparrow)-down (\downarrow)-up (\uparrow)-down (\downarrow) in the layers and the direction of V=O is severely shifted from the [001] direction. In this way, the coordination number of lithium decreases from 6 in α -, ϵ -, and $\delta\text{-V}_2\text{O}_5$ to about 4 in $\gamma\text{-V}_2\text{O}_5$, which is favorable for the lithium accommodation of V_2O_5 .

Upon on further deep discharge (lithiation), rock salt $\omega\text{-Li}_x\text{V}_2\text{O}_5$ ($2 < x \leq 3$) is formed with a voltage plateau at ~ 1.8 V (vs. Li^+/Li).^[88] As shown in Figure 3(c), oxygen completely occupies

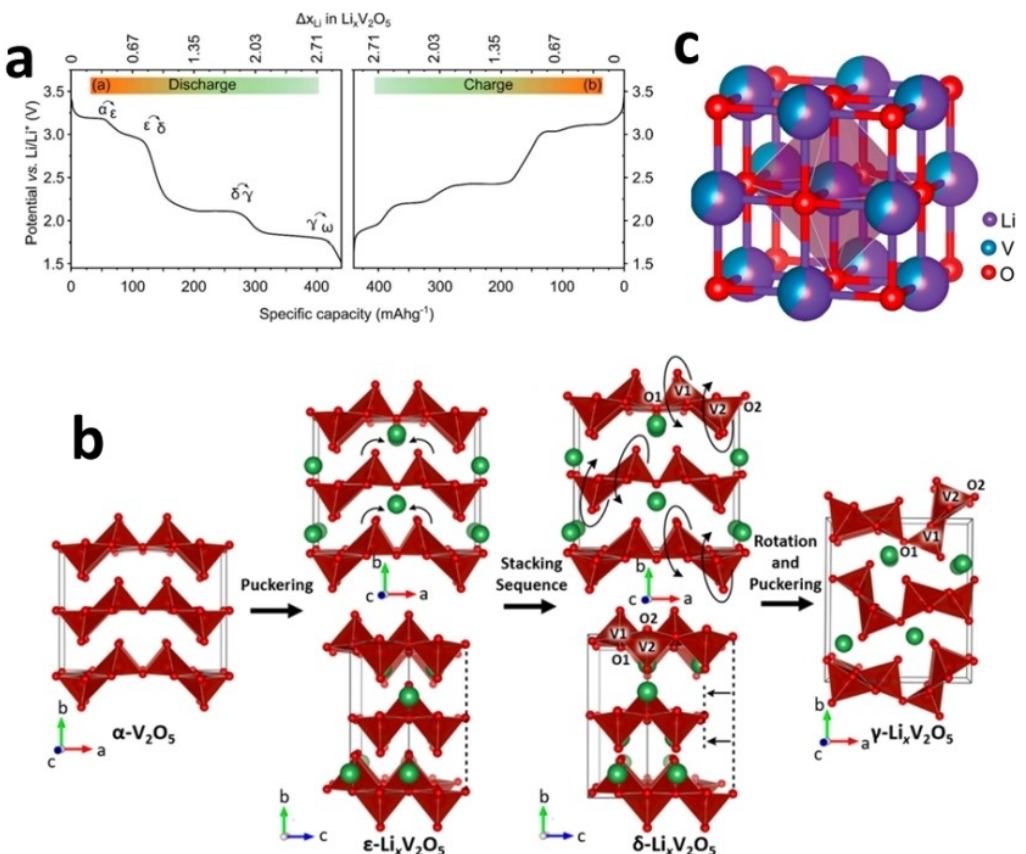


Figure 3. a) First galvanostatic discharge (left hand side)–charge (right hand side) potential profile of $\alpha\text{-V}_2\text{O}_5$ electrode in 1 M $\text{LiCl} + 1 \text{ M LiClO}_4$ in 1:3 mixture of water and acetonitrile at C/10 rate ($1 \text{ C} = 440 \text{ mAh g}^{-1}$). Reproduced with permission from Ref. [81]. Copyright (2022) The Royal Society of Chemistry. b) Sequence of lithiation-induced structural transformations of $\alpha\text{-V}_2\text{O}_5$. Reproduced with permission from Ref. [85]. Copyright (2018) American Chemical Society. c) Crystal structure of $\omega\text{-Li}_3\text{V}_2\text{O}_5$. Reproduced with permission from Ref. [89]. Copyright (2021) Wiley-VCH GmbH.

the 4a sites while the octahedral 4b sites are filled by lithium and vanadium in the form of $[VO_6]$ and $[LiO_6]$. These octahedrons are randomly arranged in this structure.^[89,90] Many reports claimed that ω - $Li_xV_2O_5$ was an irreversible reconstructive phase from which not all lithium can be extracted and α - V_2O_5 cannot be restored.^[82,91] However, the latest research shows that the electrochemical reversibility of V_2O_5 upon lithium insertion/extraction is highly size-dependent. That is, reducing the particle size of V_2O_5 could enable the reversible transformation from ω - $Li_3V_2O_5$ into α - V_2O_5 through electrochemical lithium extraction (Figure 3a).^[81,92,93]

3.2. Sodium-ion batteries

α - V_2O_5 has also been reported as electrode materials for NIBs.^[94,95] As the ionic radius of sodium is larger than that of lithium (1.02 Å vs. 0.76 Å), the structure evolution of α - V_2O_5 behaves differently during sodium storage, which has been revealed by Ali *et al.*^[96] through *ex situ* X-ray diffraction (XRD) and X-ray absorption spectroscopy (XAS) technologies. As shown in Figure 4(a), the shape of the charge-discharge curves is smooth in the voltage range of 1.2–4.0 V (vs. Na^+/Na). At the end of sodium insertion (1.2 V vs. Na^+/Na), α - V_2O_5 transforms into the mixed products consisting of major phase NaV_2O_5 and minor phase $Na_2V_2O_5$. NaV_2O_5 belongs to space group $Pmmn$ ($a=11.369$ Å, $b=3.624$ Å, $c=4.822$ Å), which is similar with α - V_2O_5 . Na-ions are located between the interlayers stacked along the c direction.^[97] The $[V_2O_5]$ sheets expand along the [001]

direction and the volume of unit cell increases by 9.2 %. $Na_2V_2O_5$ displays both crystalline and amorphous structure, which is caused by the large size of Na-ions. The crystalline $Na_2V_2O_5$ has a higher d -spacing of 5.835 Å compared with that of NaV_2O_5 . During sodium extraction, α - V_2O_5 reappears with the original crystal structure and a minor phase NaV_2O_5 is retained at the end of the desodiation process (4.0 V vs. Na^+/Na).

γ' - V_2O_5 (Figure 4b) with orthorhombic symmetry and space group $Pnma$ ($a=9.94$ Å, $b=3.58$ Å, $c=10.04$ Å) has the topological structure of α - V_2O_5 .^[98] It is made of distorted and edge-sharing $[VO_5]$ units with the period of up (\uparrow)-down (\downarrow) alternatively along the a -direction. γ' - V_2O_5 has a larger interlayer spacing of 5.02 Å compared with that of α - V_2O_5 (4.4 Å), which is favorable for sodium accommodation. The structure evolution of γ' - V_2O_5 during sodium insertion/extraction has been investigated by Baddour-Hadjean *et al.*^[98] As shown in Figure 4(c), in the voltage range of 4.00–1.75 V (vs. Na^+/Na), γ' - V_2O_5 displays a specific discharge capacity of ~147 mAhg⁻¹, corresponding to 1 eq. sodium per V_2O_5 formula unit. Only one potential plateau is observed at 3.3 V (vs. Na^+/Na), indicating a two-phase reaction of the material during sodium insertion. At the end of sodium insertion, a well-crystallized layered γ - $Na_{0.97}V_2O_5$ bronze with orthorhombic symmetry and $Pnma$ space group is formed with Na-ions located at the octahedral sites between the interlayers (Figure 4d).^[99] Although γ - $Na_{0.97}V_2O_5$ has the isomorphic structure to γ - LiV_2O_5 , it exhibits a higher c value ($a=9.76$ Å, $b=3.63$ Å, $c=11.95$ Å) compared with that of γ - LiV_2O_5 (10.66 Å) due to the relatively larger ionic radius of sodium.^[100] During the repeated charge-discharge processes, a

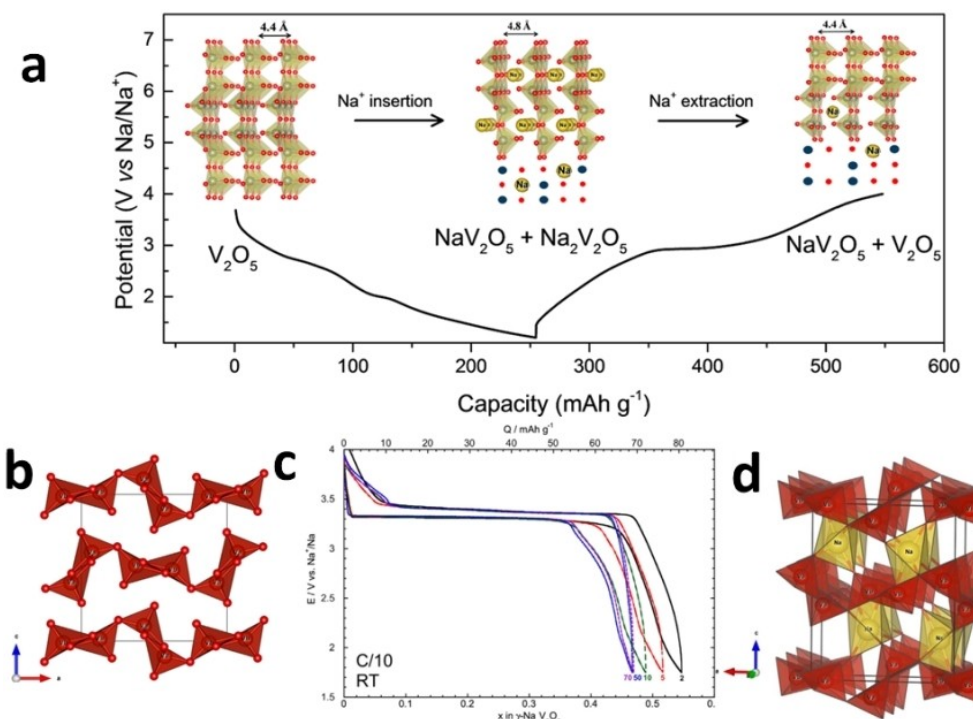


Figure 4. a) Crystal structure of V_2O_5 , showing sodium-ions de/intercalation channels along with charge-discharge potential profiles. R reproduced with permission from Ref. [96]. Copyright (2016) American Chemical Society. b) Crystal structure of γ' - V_2O_5 . c) Discharge-charge cycling curves of γ' - V_2O_5 at room temperature. Reproduced with permission from Ref. [98]. Copyright (2017) Elsevier Ltd. d) Crystal structure of γ - $Na_{0.97}V_2O_5$. Dark line indicates the orthorhombic cell ($Pnma$ space group; $Z = 4$). Reproduced with permission from Ref. [99]. Copyright (2017) Elsevier Inc.

reversible transition between $\gamma\text{-Na}_{0.97}\text{V}_2\text{O}_5$ and $\gamma'\text{-V}_2\text{O}_5$ occurs, which has also been reported for sodium pre-intercalated V_2O_5 by Emery et al.^[101]

3.3. Potassium-ion batteries

The electrochemical insertion of K-ions into $\alpha\text{-V}_2\text{O}_5$ is rather difficult because of the much bigger ionic radius of potassium (1.37 Å) compared with that of lithium (0.76 Å) and sodium (1.02 Å).^[102,103] As shown in Figure 5(a), in the voltage range of 1.5–4.0 V (vs. K^+/K) and under a slow rate of C/12 (1 C = 295 mAh g⁻¹), $\alpha\text{-V}_2\text{O}_5$ nanoparticles exhibit initial potassiation and depotassiation capacities of 200 mAh g⁻¹ and 217 mAh g⁻¹, respectively. During the first potassiation, about 1.36 equiv. of K-ions could be inserted per V_2O_5 unit with about 3/4 capacity being achieved below 2.0 V (vs. K^+/K), which may be attributed to the huge potassiation resistance. The first potassiation voltage profile can be divided into two regions, namely Region I with voltage above 2.0 V (vs. K^+/K) and Region II with voltage below 2.0 V (vs. K^+/K). $\text{K}_{0.6}\text{V}_2\text{O}_5$ is formed through a solid solution reaction in Region I. The lattice parameter a is slightly changed while lattice parameters b and c are significantly increased (Figure 5b). In Region II, a new phase Ph1 ($\text{pmn}2_1$, $a = 11.128 \text{ \AA}$, $b = 8761 \text{ \AA}$, $c = 3.326 \text{ \AA}$) is formed by a two-phase reaction (Figure 5c).

$a = 11.107 \text{ \AA}$, $b = 8.940 \text{ \AA}$, $c = 3.233 \text{ \AA}$ is generated. During the subsequent depotassiation, $\text{K}_{0.6}\text{V}_2\text{O}_5$ is transformed into $\text{K}_{0.6-\delta}\text{V}_2\text{O}_5$ by a solid-solution reaction and a new phase Ph2 ($\text{pmn}2_1$, $a = 11.128 \text{ \AA}$, $b = 8761 \text{ \AA}$, $c = 3.326 \text{ \AA}$) is formed by a two-phase reaction (Figure 5c).

As shown in Figure 5(d), the structure of $\alpha\text{-V}_2\text{O}_5$ can be reconstructed by chemical methods to enlarge the interlayer spacings for fast potassium transport.^[104] In brief, the $[\text{V}_2\text{O}_5]$ layers slip and meanwhile, the $[\text{VO}_5]$ units rotate backward during K-ions insertion. Then, the $[\text{VO}_5]$ units transform into $[\text{VO}_6]$ octahedrons by vanadium atoms rearranging and rebonding with the oxygen atoms. K-ions are sandwiched between the interlayers. The final product $\delta\text{-K}_{0.5(1)}\text{V}_2\text{O}_5$ with monoclinic symmetry and space group of $\text{C}2/m$ has a similar structure with $\text{V}_2\text{O}_5 \cdot n\text{H}_2\text{O}$. After the initial charging (depotassiation) process, all K-ions can be extracted from $\delta\text{-K}_{0.5(1)}\text{V}_2\text{O}_5$.^[105] In the following discharging (potassiation) process, ~1 eq. potassium could be reversibly inserted per V_2O_5 unit (Figure 5e and f). $\delta\text{-K}_{0.5(1)}\text{V}_2\text{O}_5$ undergoes three stages (stage I, stage II, and stage III) during K-ions insertion/extraction. In stage I, $\delta\text{-V}_2\text{O}_5$ is transformed into $\delta\text{-K}_x\text{V}_2\text{O}_5$ with all patterns remained. In stage II, $\delta\text{-K}_x\text{V}_2\text{O}_5$ disappears and a new phase ($n\text{-K}_x\text{V}_2\text{O}_5$) is generated. This $n\text{-K}_x\text{V}_2\text{O}_5$ phase has a bilayered structure with monoclinic symmetry and space group $\text{C}2/m$, which is stable

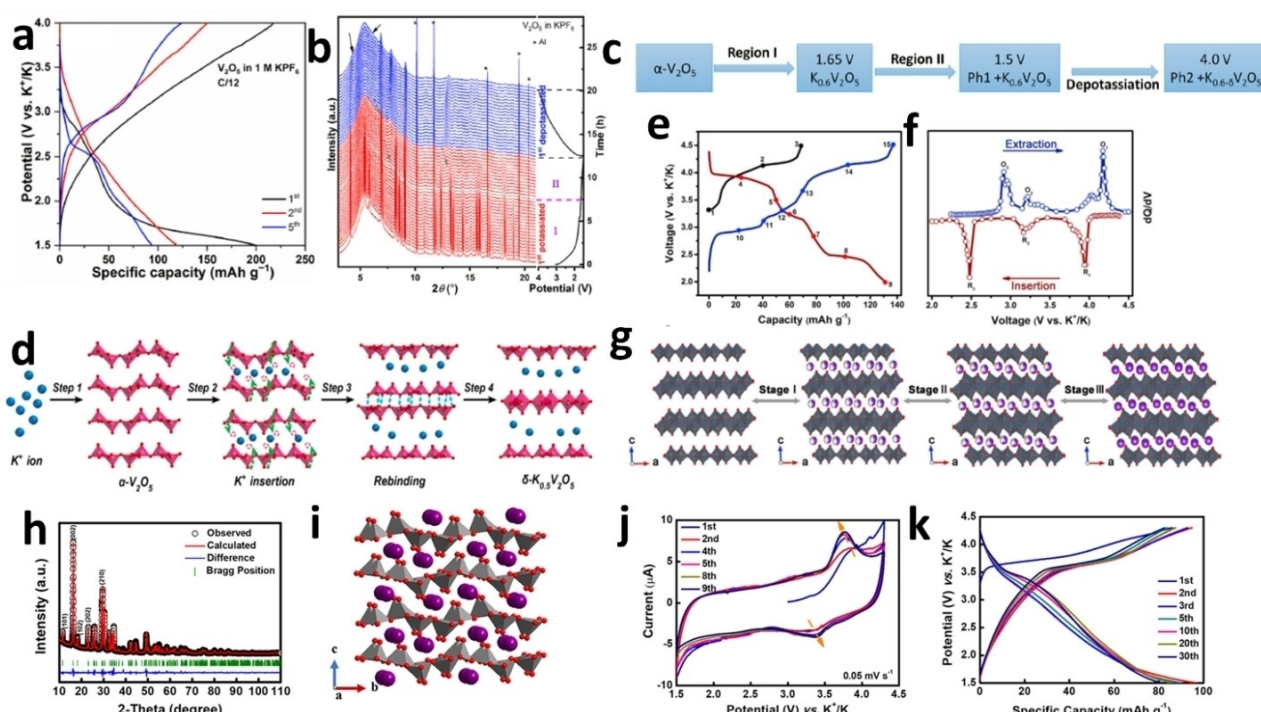


Figure 5. a) Potassiation-depotassiation potential profiles of V_2O_5 nanoparticles in 1 M KPF_6/PC electrolyte at a rate of C/12 (1 C = 295 mAh g⁻¹). (b) *In operando* synchrotron diffraction of V_2O_5 during the first K-insertion/extraction cycle and the corresponding voltage profile at a rate of C/15 (cell was running at C/30 for the first 5.4 h) indicating Region I, Region II, and depotassiation. c) Phase changes of V_2O_5 during the 1st cycle. Reproduced with permission from Ref. [178]. Copyright (2021) Elsevier B.V. d) Schematic diagrams of the structural evolution from $\alpha\text{-V}_2\text{O}_5$ to $\delta\text{-K}_{0.5}\text{V}_2\text{O}_5$. Reproduced with permission from Ref. [104]. Copyright (2021) American Chemical Society. e) Galvanostatic charge-discharge potential curves of $\delta\text{-K}_{0.5}\text{V}_2\text{O}_5$ and f) the corresponding $d\text{Q}/d\text{V}$ curves. g) Structural evolution of $\delta\text{-K}_{0.5}\text{V}_2\text{O}_5$ upon potassium ions insertion and extraction. Reproduced with permission from Ref. [179]. Copyright (2019) Elsevier Inc. h) Rietveld-refined XRD pattern and i) illustration of the crystal structure of $\text{K}_{0.83}\text{V}_2\text{O}_5$ (purple and red balls represent K and O atoms), respectively (for concision, V atoms are not shown here). j) CV profiles at a scan rate of 0.05 mV s⁻¹ between 1.5 and 4.3 V (vs. K^+/K) and k) galvanostatic charge-discharge profiles. Reproduced with permission from Ref. [106]. Copyright (2020) American Chemical Society.

during K-ions accommodation. In stage III, the potassium content is increased from $n\text{-K}_2\text{V}_2\text{O}_5$ to $n\text{-KV}_2\text{O}_5$ by a solid-solution reaction (Figure 5g). The interlayer spacing of the fully discharged product $n\text{-KV}_2\text{O}_5$ (9.0 Å) is smaller than that of fully charged one $\delta\text{-V}_2\text{O}_5$ (9.4 Å). This phenomenon may be attributed to the presence of K-ions in the interlayers, which attract oxygen atoms of adjacent $[\text{V}_2\text{O}_5]$ bilayers by electrostatic interaction.

Recently, our group reported a potassium-rich phase $\text{K}_{0.83}\text{V}_2\text{O}_5$ as a cathode material for KIBs.^[106] This $\text{K}_{0.83}\text{V}_2\text{O}_5$ phase is synthesized by chemical potassiation of $\gamma\text{-V}_2\text{O}_5$, which is obtained by chemical oxidation of $\gamma\text{-LiV}_2\text{O}_5$. The Rietveld refinement of the powder X-ray diffraction pattern indicates that $\text{K}_{0.83}\text{V}_2\text{O}_5$ has an orthorhombic symmetry with space group *Pnma* and lattice parameters of $a = 3.73$ Å, $b = 10.95$ Å, $c = 10.93$ Å (Figure 5h). In $\text{K}_{0.83}\text{V}_2\text{O}_5$, the $[\text{VO}_5]$ square pyramids are edge- and corner-shared to form double strings along the a -axis (Figure 5i). Along the b -axis, these strings are corner-shared to form the puckered $[\text{V}_2\text{O}_5]$ layers. Along the c -axis, these puckered $[\text{V}_2\text{O}_5]$ layers are perpendicularly stacked to generate the layered structure with K-ions located between the layers. Compared with $\alpha\text{-V}_2\text{O}_5$ which is the precursor for $\delta\text{-K}_{0.5}\text{V}_2\text{O}_5$, $\gamma\text{-V}_2\text{O}_5$ as the precursor for $\text{K}_{0.83}\text{V}_2\text{O}_5$ exhibits a slightly larger $[\text{V}_2\text{O}_5]$ interlayer spacing. Therefore, for $\alpha\text{-V}_2\text{O}_5$, potassium insertion occurs at every two $[\text{V}_2\text{O}_5]$ layers to mitigate the insertion-induced stress and meanwhile, reversal, slip, and rebonding of the $[\text{VO}_5]$ square pyramids take place between the adjacent layers to generate the $[\text{VO}_6]$ octahedrons in $\delta\text{-K}_{0.5}\text{V}_2\text{O}_5$. In contrast, benefitting from the slightly larger interlayer distance, potassium insertion can be realized between every puckered $[\text{V}_2\text{O}_5]$ layer in $\gamma\text{-V}_2\text{O}_5$, which allows more potassium to be introduced into $\gamma\text{-V}_2\text{O}_5$ to form the potassium-rich phase $\text{K}_{0.83}\text{V}_2\text{O}_5$. Interestingly, although $\text{K}_{0.83}\text{V}_2\text{O}_5$ is prepared through chemical potassiation of $\gamma\text{-V}_2\text{O}_5$, its crystalline structure is more similar with $\alpha\text{-V}_2\text{O}_5$ instead of $\gamma\text{-V}_2\text{O}_5$. Electrochemical performance-wise, in the voltage range of 1.5–4.3 V (vs. K^+/K), about 0.68 eq. K-ions could be reversibly extracted and re-inserted per V_2O_5 unit, corresponding to a specific capacity of 85 mAh g^{-1} , with a couple of voltage plateaus at 3.6 and 3.4 V (vs. K^+/K) during the charge and discharge processes, respectively (Figure 5j and k). The depotassiation-potassiation process of $\text{K}_{0.83}\text{V}_2\text{O}_5$ is unveiled to be accompanied by varying the puckering degree of $[\text{V}_2\text{O}_5]$ layers, which provides flexibility to mitigate the depotassiation-potassiation induced strain and helps achieve stable cycling performance for the material. During the depotassiation process, the valence state change of vanadium from +4 to +5 causes the a -axis lattice to shrink by 4.2%. The loss of potassium pillar between the interlayers results in a 15.2% reduction for the c -axis lattice while the b -axis lattice increases by 5.5% due to the unpuckering of the $[\text{V}_2\text{O}_5]$ layers induced by the reduced interaction between potassium and oxygen. Thus, the depotassiation process is accompanied by a unit cell volume reduction of 14.2%. Upon potassiation process, the aforementioned lattice parameters change is completely reversed. It is worth noting that stable $\alpha\text{-V}_2\text{O}_5$ forms after potassium ions are completely extracted from $\text{K}_{0.83}\text{V}_2\text{O}_5$ and it is inactive in the subsequent cycles.

3.4. Magnesium-ion batteries

Besides the classical Chevrel phase Mo_6S_8 , single layered V_2O_5 has been considered as a promising electrode material for MIBs. However, due to the divalent and highly polarizable nature of Mg-ions, the Mg–O interaction is quite strong and the transport of Mg-ions inside V_2O_5 is very slow, which causes a low practical capacity and poor rate performance. Zhou et al.^[107] reported that the diffusion barrier of Mg-ions in $\alpha\text{-V}_2\text{O}_5$ (1.26 eV) was more than three times higher than that of Li-ions (0.35 eV) despite the relatively smaller size of Mg-ions compared with Li-ions (0.66 Å vs. 0.76 Å). Both experimental characterizations and theoretical calculation have confirmed that $\alpha\text{-V}_2\text{O}_5$ is transformed into $\epsilon\text{-Mg}_{0.5}\text{V}_2\text{O}_5$ at the end of magnesium insertion.^[108,109] As shown in Figure 6(a), $\epsilon\text{-Mg}_{0.5}\text{V}_2\text{O}_5$ is half magnesiation and the Mg-ions are alternately inserted into the interlayer space along with the [010] direction.

As shown in Figure 6(b), $\alpha\text{-V}_2\text{O}_5$ exhibits a specific capacity of 40 mAh g^{-1} during Mg-ions insertion, corresponding to about 0.27 equiv. of Mg-ions inserted per V_2O_5 unit, which is much lower than that of lithium (~2 Li-ions per V_2O_5 unit). Yoo et al.^[110] found that high temperature can enhance the kinetics of Mg-ions insertion. The reversible capacity of $\alpha\text{-V}_2\text{O}_5$ increases to $\sim 280 \text{ mAh g}^{-1}$ at 100°C , which is corresponding to 1 equiv. of Mg-ions stored per V_2O_5 unit. At the end of magnesium insertion under high temperature, the fully magnesiated phase $\delta\text{-MgV}_2\text{O}_5$ is formed, which possesses an orthorhombic symmetry with space group *Pmmn*. The $\delta\text{-MgV}_2\text{O}_5$ phase consists of corner-sharing $[\text{VO}_5]$ polyhedrons containing V^{4+} ions with Mg-ions coordinated by six O atoms between the interlayers.^[111,112] First principles calculations demonstrate that magnesium pre-intercalated $\alpha\text{-V}_2\text{O}_5$ may be a potential cathode material for MIBs due to the reduced diffusion barriers of Mg-ions.^[113]

Besides increasing temperature, reducing the particle size is also favorable for kinetics enhancement. Gershinsky and co-workers^[114] found that $\alpha\text{-V}_2\text{O}_5$ film prepared from particles with size of 20–50 nm could deliver a discharge capacity of 150 mAh g^{-1} which is equivalent to about 0.5 equiv. of magnesium inserted per V_2O_5 unit (Figure 6c).

$\beta\text{-V}_2\text{O}_5$ also has a layered structure and can be synthesized from $\alpha\text{-V}_2\text{O}_5$ under high pressure (4.0–6.0 GPa) and high temperature (~ 900 K) (Figure 7a). It has a monoclinic symmetry with space group *P21/m* and lattice parameters of $a = 7.1140$ Å, $b = 3.5718$ Å, $c = 6.2846$ Å^[115]. The 2D layers are formed by infinite chains which are built up of edge-shared $[\text{VO}_6]$ quadruple units along the b -axis. These chains are linked by corner-sharing between $[\text{VO}_6]$ along the c -axis to form the $[\text{V}_4\text{O}_{10}]$ layers.^[116,117] As shown in Figure 7(b and c), ~ 1.2 Mg-ions could be reversibly accommodated per V_2O_5 formula unit, corresponding to a specific capacity of 361 mAh g^{-1} , and Mg-ions experience a lower diffusion barrier in $\beta\text{-V}_2\text{O}_5$.^[118]

$\xi\text{-V}_2\text{O}_5$ is a metastable phase with a distinctive 1D tunnel structure, which is significantly different with that of $\alpha\text{-V}_2\text{O}_5$ and $\text{V}_2\text{O}_5\cdot n\text{H}_2\text{O}$ (Figure 7d). Andrews et al.^[119] found that 0.33 equiv. of Mg-ions could be reversibly inserted per V_2O_5 formula unit (Figure 7e), which is accompanied by a small volume expansion from 522.96 to 525.63 Å³ ($\sim 0.51\%$). In the magnesiated $\xi\text{-V}_2\text{O}_5$,

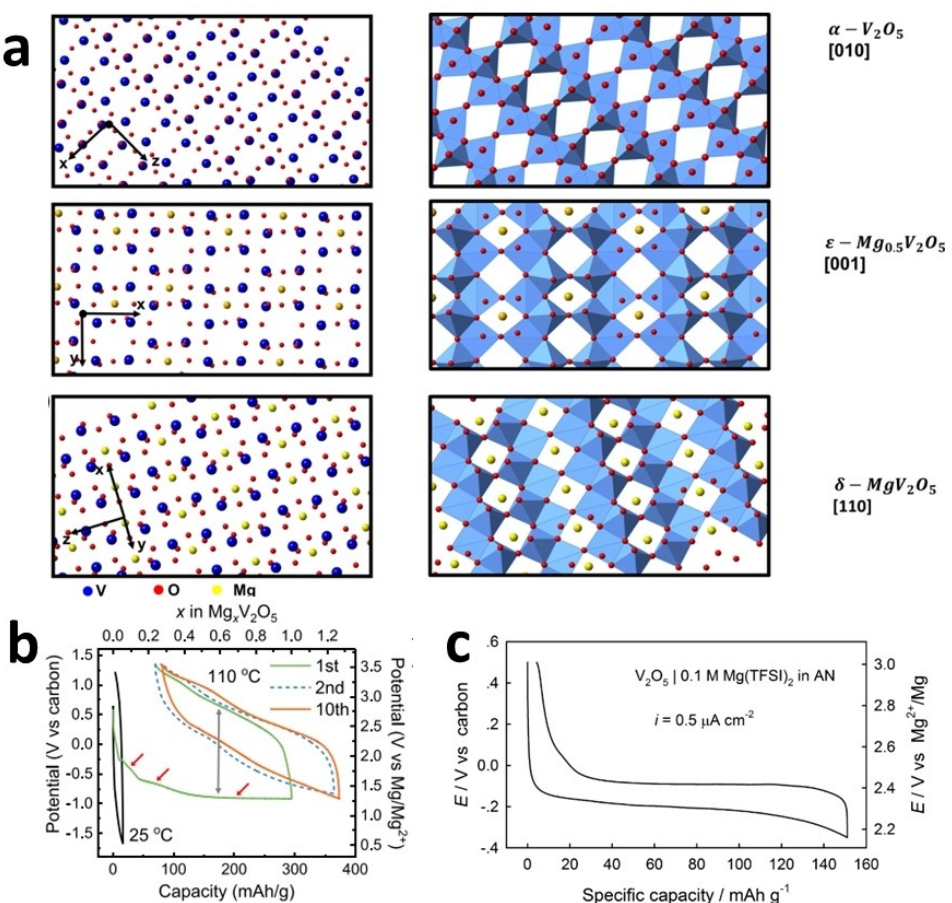


Figure 6. a) Structural models of $\alpha - V_2 O_5$, $\varepsilon - Mg_{0.5} V_2 O_5$, and $\delta - MgV_2 O_5$. Reproduced with permission from Ref. [108]. Copyright (2017) American Chemical Society. b) Voltage profiles of the electrochemical cycling of $\alpha - V_2 O_5$ in an ionic liquid electrolyte at 25 °C and 110 °C. Reproduced with permission from Ref. [110]. Copyright (2019) American Chemical Society. c) Typical galvanostatic titration curve of a $V_2 O_5$ thin-film electrode in 0.1 M $Mg(\text{TFSI})_2$ in acetonitrile (current density = 0.5 $\mu\text{A cm}^{-2}$). Reproduced with permission from Ref. [114]. Copyright (2013) American Chemical Society.

Mg-ions occupy the β or β' sites forming $\beta - Mg_x V_2 O_5$ or $\beta' - Mg_x V_2 O_5$. The coordination numbers of Mg-ions in $\beta - Mg_x V_2 O_5$ and $\beta' - Mg_x V_2 O_5$ are 5 and 4, respectively. The coordination number of Mg-ions in $\varepsilon - V_2 O_5$ varies as following: 5 (β sites) \rightarrow 3 \rightarrow 4 (β' sites) \rightarrow 3 \rightarrow 5 (β sites) during the insertion process.

3.5. Zinc-ion batteries

$\alpha - V_2 O_5$ has been frequently used as a cathode material in the aqueous ZIBs.^[120–122] It has been confirmed that during the discharge process of aqueous ZIBs, the hydrated Zn-ions will be inserted into the interlayer space of $V_2 O_5$, during which the hydration sheath of Zn-ions plays a critical role in reducing the electrostatic interactions between Zn-ions and the host structure and facilitating the Zn-ions diffusion. However, the structure evolution of $\alpha - V_2 O_5$ during Zn-ions insertion is ambiguous, which is attributed to the acidic environment of the electrolyte.^[123]

Chen et al.^[124] reported the structure evolution of $\alpha - V_2 O_5$ during Zn-ions insertion using aqueous $Zn(CF_3SO_3)_2$ as the

electrolyte in the voltage range of 0.5–1.5 V (vs. Zn^{2+}/Zn). As shown in Figure 8(a), at the end of discharge (zinc insertion) process, phase transition from $\alpha - V_2 O_5$ to $Zn_{3+x}(OH)_2 V_2 O_7 \cdot 2H_2O$ (JCPDS No. 50–570) takes place, which is similar with Lu's results.^[125] It has a layered structure, which is built of $[VO_4]$ tetrahedrons with Zn-ions located at the interlayer space forming $[ZnO_6]$ octahedrons and H_2O molecules randomly distributed in the large interlayer. During the subsequent charge (zinc extraction) process, Zn-ions are reversibly extracted from $Zn_{3+x}(OH)_2 V_2 O_7 \cdot 2H_2O$ with a reversible capacity of 319 mAh g^{-1} . During the following cycles, $\alpha - V_2 O_5$ is not restored and the redox reaction is accompanied by reversible insertion-extraction of Zn-ions in the open-structured host $Zn_{3+x}(OH)_2 V_2 O_7 \cdot 2H_2O$.

In contrast with previous studies, Zhang et al.^[126] found that $\alpha - V_2 O_5$ transformed into double layered $Zn_x V_2 O_5 \cdot nH_2O$, when deeply discharged to 0.2 V (vs. Zn^{2+}/Zn) (Figure 8b and c). The interlayer spacing increases from 4.4 Å of $\alpha - V_2 O_5$ to 13.4 Å of $Zn_{1.6} V_2 O_5 \cdot nH_2O$ due to the co-intercalation of Zn-ions and water molecules. During the following cycles, hydrated Zn-ions are reversibly extracted from $Zn_x V_2 O_5 \cdot nH_2O$ and the pristine $\alpha - V_2 O_5$ structure reappears. Electrochemically, 1.6 equiv. of Zn-ions can

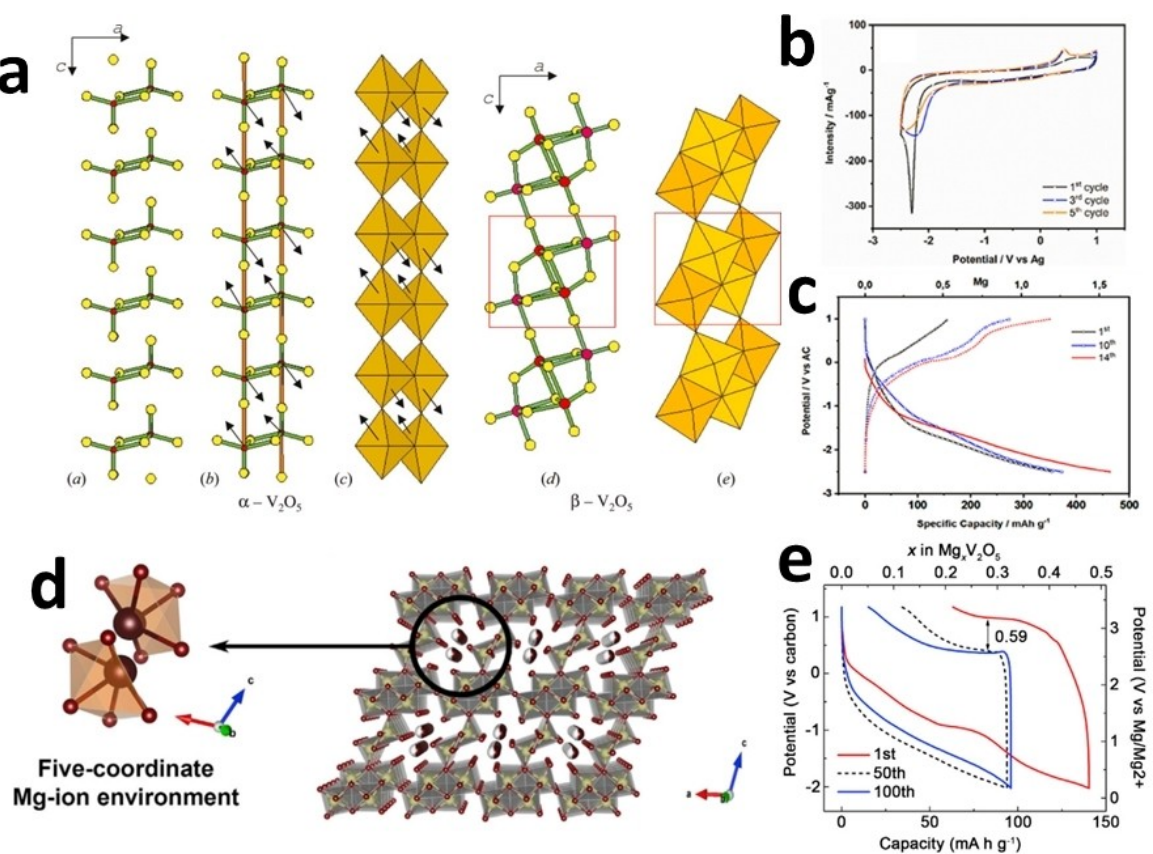


Figure 7. a) Hypothetical model showing the transformation from α - V_2O_5 to β - V_2O_5 . The arrows indicate the formation of the crystallographic shear groups. Reproduced with permission from Ref. [115]. Copyright (2004) International Union of Crystallography. b) Selected cyclic voltammetry and c) reduction/oxidation cycles in galvanostatic mode for β - V_2O_5 using 0.1 $Mg(ClO_4)_2$ in acetonitrile as electrolyte. AC = activated carbon. Reproduced with permission from Ref. [118]. Copyright (2022) American Chemical Society. d) A refined structure of the chemically magnesiated ξ - V_2O_5 phase where magnesium resides in a pseudo-square-pyramidal β site. e) Voltage versus capacity profiles acquired at different cycle numbers for the electrochemical cycling of ξ - V_2O_5 . Reproduced with permission from Ref. [119]. Copyright (2017) Elsevier Inc.

be reversibly inserted and extracted per V_2O_5 formula unit, corresponding to a reversible specific capacity of 470 $mAh g^{-1}$. Recently, Liu et al.^[127] performed *in situ* XRD to clarify the Zn storage mechanism in α - V_2O_5 . They discovered that $Zn_xV_2O_5$ firstly formed by Zn-ions intercalation through a solid-solution reaction during the initial discharge (Figure 8d). After that, Zn-ions and H₂O co-intercalated the interlayer of $Zn_xV_2O_5$. Such a process proceeded through a typical two-phase reaction and $Zn_xV_2O_5 \cdot nH_2O$ was generated at the end of discharge. The subsequent discharge-charge cycles were based on the following reversible phase transition: $V_2O_5 \leftrightarrow Zn_xV_2O_5 \leftrightarrow Zn_xV_2O_5 \cdot nH_2O$. A more detailed structure evolution was proposed by Byeon et al.^[128] using atomic-column-resolved scanning transmission electron microscopy. The intercalation of both H₂O and Zn-ions into the interlayer of V_2O_5 was directly visualized. During the intercalation process, Zn-ions placed at the pyramidal interstitial sites and H₂O molecules intercalated into double-trigonal interstitial sites, resulting in the formation of VO₂(A)- and VO-rock salt-type intermediate phases.

Recent research shows that the above difference regarding the products at the end of Zn-ions insertion is related with the transformation of α - V_2O_5 into VO₂(OH)₂⁻ species caused by the

acidic electrolyte (aqueous $Zn(CF_3SO_3)_2$).^[129] For example, when α - V_2O_5 is tested at high C rate, the structure transformation of V_2O_5 is truly based on $V_2O_5 \leftrightarrow Zn_xV_2O_5 \leftrightarrow Zn_xV_2O_5 \cdot nH_2O$ during the initial several cycles. However, with the electrochemical testing going on, $V_2O_5 \cdot nH_2O$ ($Zn_xV_2O_5 \cdot nH_2O$) transforms into VO₂(OH)₂, which further reacts with Zn-ions to form Zn₃(VO₂)₂(OH)₂(H₂O)₂. The structure transformation mode switches to reversible insertion-extraction of Zn-ions in Zn_{3+x}(OH)₂V₂O₇·2H₂O.

Intercalating water or big organic molecules into the interlayers of α - V_2O_5 may lead to the structure transformation from single layer to double layer. Yao et al.^[130] *in situ* polymerized 3,4-ethylenedioxythiophene (PEDOT) between the interlayers of α - V_2O_5 and the interlayer spacing of α - V_2O_5 was enlarged at the surface. The *d*-spacing of the intercalated V_2O_5 is identified as 9.86 Å, which is consistent with the characteristics of α - V_2O_5 expanded by monolayer PEDOT. The intercalation of PEDOT suppresses the dissolution of V_2O_5 and triggers the unprecedented structure stability of material during the Zn-ions insertion-extraction. A stable specific discharge (Zn-ion insertion) capacity of 269 $mAh g^{-1}$ is achieved after 4500 cycles at 10 Ag^{-1} . “Synergic lattice breathing mechanism” is proposed for the Zn-ion accommodation (Figure 8e). Namely, during the

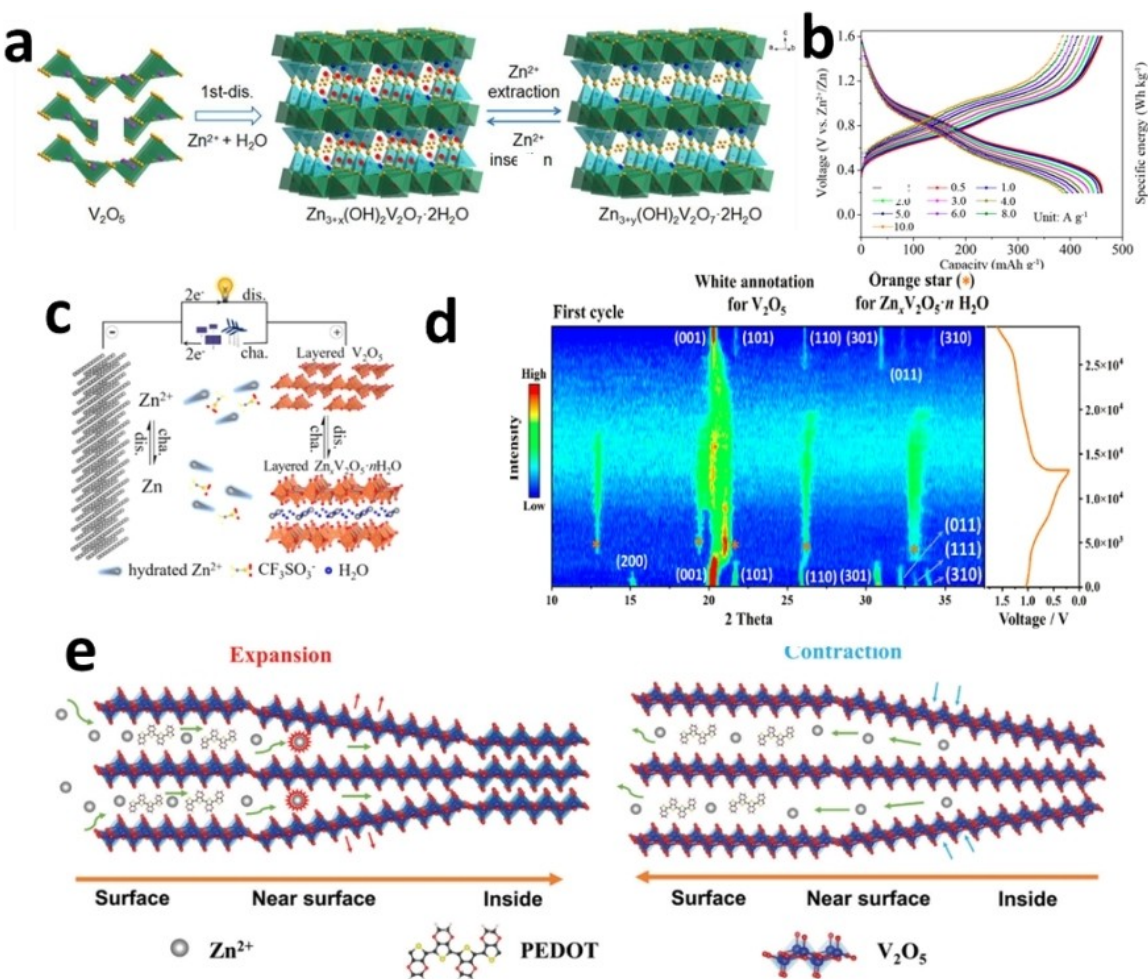


Figure 8. a) Schematic illustration of the insertion of zinc-ions into α -V₂O₅. Reproduced with permission from Ref. [124]. Copyright (2019) Elsevier B.V. b) The discharge-charge potential profiles of Zn–V₂O₅ battery at various current densities. c) Schematic illustration of the rechargeable aqueous Zn–V₂O₅ battery. Reproduced with permission from Ref. [126]. Copyright (2018) American Chemical Society. d) Contour plot of *in situ* XRD characterization with corresponding voltage profile of α -V₂O₅ during zinc-ion insertion/extraction. Reproduced with permission from Ref. [127]. Copyright (2022) American Chemical Society. e) Schematic illustration of the "synergistic lattice breathing" mechanism for V₂O₅ interlayer expansion and contraction. Reproduced with permission from Ref. [130]. Copyright (2020) The Royal Society of Chemistry.

Zn-ion insertion, a sequential expansion of interlayer spacing occurs from the outer PEDOT-pillared V₂O₅ shell to the inner core. During the Zn-ion extraction, contraction of the interlayer spacing is initiated from the inner interlayer and spreads to the outer part.

3.6. Calcium-ion batteries

Among the various ions listed in Table 1 which are used as charge carriers for metal-ion batteries, calcium has the second lowest standard redox potential (-2.87 V vs. SHE) after lithium, indicating that CIBs may have high output voltage similar with LIBs.^[131] Moreover, calcium has the second largest ionic radius after potassium, which results in a low surface charge density and weak interaction between Ca-ions and solvent, benefitting the transport kinetics of Ca-ions in electrolyte. It has been shown that α -V₂O₅ would react with the various electrolytes

used in CIBs during the calcium insertion. As shown in Figure 9(a), the galvanostatic charge-discharge curves of α -V₂O₅ in CIBs are closely related to the type of electrolytes. Due to the complex reactions between α -V₂O₅ and electrolytes, the structure evolution of α -V₂O₅ during Ca-ions intercalation has not been systematically studied by experimental methods.^[132,133]

Wang and co-workers^[134] investigated the structure evolution of α -V₂O₅ during Ca-ions intercalation using density functional theory (DFT) calculations. As shown in Figure 9(b), α -V₂O₅ experiences two stages, namely Stage I and Stage II, during the Ca-ions intercalation. Stage I is defined as that Ca-ions are located at a single gallery of α -V₂O₅ while Ca-ions occupy all galleries in Stage II. The difference between Stage I and Stage II can be explained as the competition between interlayer van der Waals interaction and ion–ion Coulombic repulsion. As shown in Figure 9(c), the reaction mechanism during Ca-ions intercalation is calculated as following:

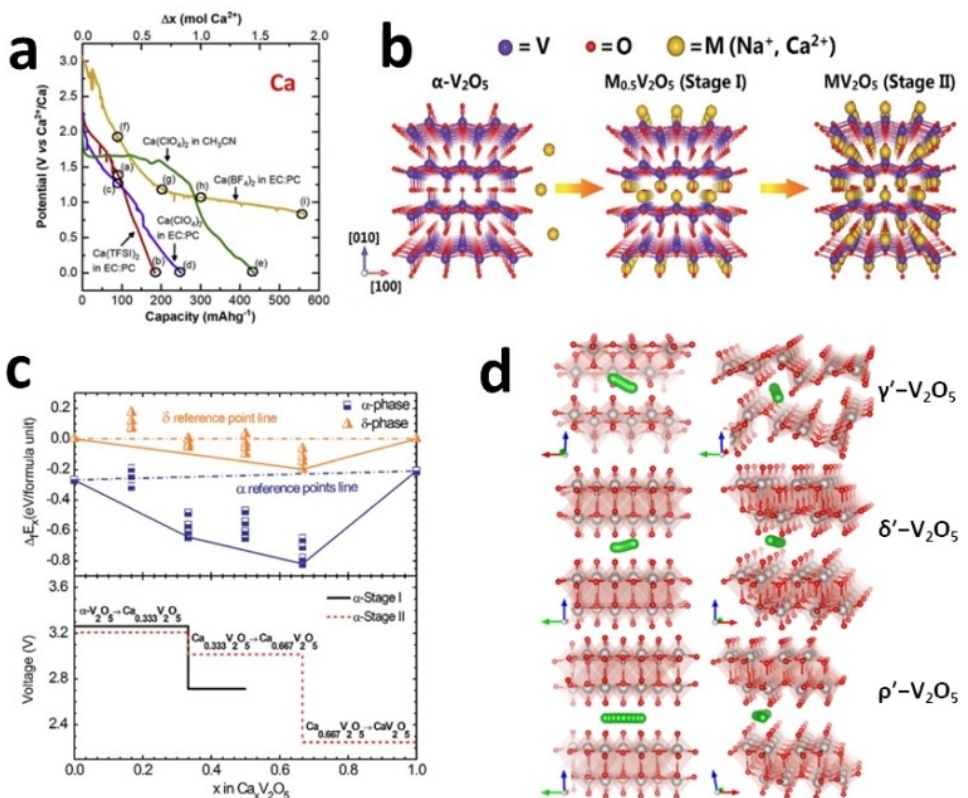
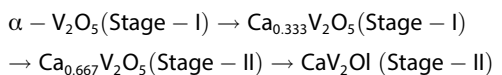


Figure 9. a) Galvanostatic charge-discharge curves of α -V₂O₅. Reproduced with permission from Ref. [180]. Copyright (2018) Elsevier B.V. b) Schematic illustration of the stage I and stage II arrangements of calcium storage in α -V₂O₅. c) The formation energies per formula unit and the voltages of α - and δ -V₂O₅ are shown as a function of calcium concentration. Reproduced with permission from Ref. [134]. Copyright (2016) The Royal Society of Chemistry. d) Migration pathways for the Ca-ions in different host structures. Reproduced with permission from Ref. [135]. Copyright (2017) American Chemical Society.



The energy barriers of calcium diffusion in α -V₂O₅ are estimated to be 0.975–1.825 eV. The structural parameters of calcium-intercalated intermediates are summarized in Table 2.

Parija et al.^[135] explored the structure evolution of the metastable γ' -V₂O₅, δ' -V₂O₅, and ϱ' -V₂O₅ during Ca-ions intercalation. As shown in Figure 9(d), γ' -V₂O₅ has a single layered structure while δ' - and ϱ' -V₂O₅ possess a bilayered structure. The coordination number of the Ca-ion varies as the order of 5 → 3 → 4 → 3 → 5 during its diffusion in γ' - and δ' -V₂O₅. While it follows the sequence of 6 → 4 → 6 → 4 → 6 in ϱ' -V₂O₅. α -V₂O₅ has the oxygen coordination number sequence of 8 → 3 → 8. The DFT calculation results indicate that the diffusion barriers of Ca-ions in the metastable γ' -, δ' -, and ϱ' -V₂O₅ are 0.59–0.68 eV, 0.56–0.65 eV, and 0.37–0.55 eV, respectively, which are lower than that in α -

V₂O₅, suggesting that V₂O₅ with γ' -, δ' - or ϱ' -phase may have improved rate performance over α -phase.

3.7. Aluminum-ion batteries

AlBs are characterized by high theoretical capacities due to the three electrons redox reactions.^[136,137] However, the electrochemical intercalation of Al-ions into the interlayer of α -V₂O₅ is difficult because of the strong electrostatic interaction between trivalent Al-ions and the host material. The accommodation of aluminum in α -V₂O₅ has been reported in recent years, while the structure evolution was barely involved.^[138,139] Gu et al.^[140] uncovered the reversible storage mechanism of Al-ions in α -V₂O₅ nanowires using metal aluminum as the reference electrode in the voltage range of 0.02–2.5 V (vs. Al³⁺/Al) at room temperature. As shown in Figure 10(a), α -V₂O₅ delivers a discharge (Al-ions intercalation) capacity of 53.4 mAh g⁻¹ in the second cycle, which is corresponding to 0.1 equiv. of aluminum inserted per V₂O₅ formula unit. There are two voltage plateaus located at ~0.6 and ~0.3 V (vs. Al³⁺/Al) during the Al-ions insertion, suggesting two phase transformation processes, which was also reported by Jayaprakash's results.^[141] During aluminum intercalation, the lattice parameters of α -V₂O₅ experience slight variations (Figure 10b and c). At the end of

Table 2. Lattice parameters for calcium intercalated α -V₂O₅^[134]

	a [Å]	b [Å]	c [Å]	α [°]	β [°]	γ [°]
α -Ca _{0.333} V ₂ O ₅	3.582	4.546	11.524	90	90	90
α -Ca _{0.667} V ₂ O ₅	3.594	4.618	11.498	90	90	90
α -CaV ₂ O ₅	3.585	4.755	11.504	90	90	90

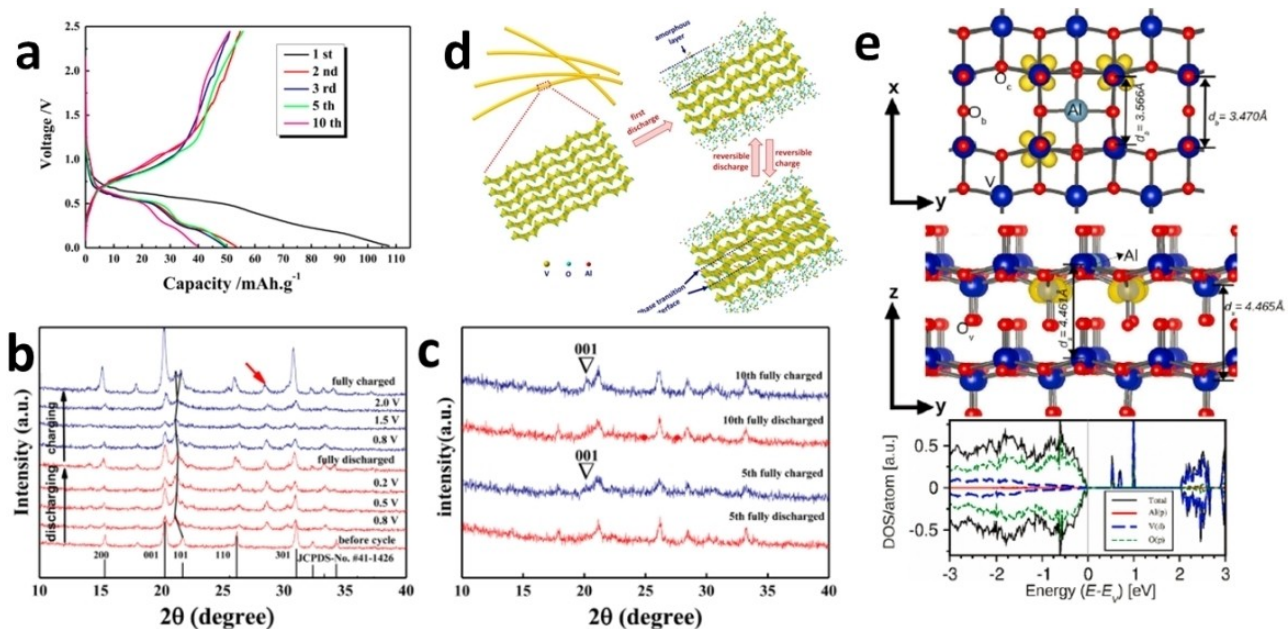


Figure 10. a) Galvanostatic charge-discharge profiles of α -V₂O₅ nanowire. *Ex situ* XRD patterns of α -V₂O₅ at various discharge and charge states b) through the first cycle and c) after the 5th and 10th cycles. d) Schematic diagram of Al-ions electrochemical insertion/extraction in crystalline V₂O₅ nanowire. Reproduced with permission from Ref. [140]. Copyright (2017) Elsevier B.V. e) V₂O₅ intra-layer intercalation (1 × 3 × 2 supercell, Al_{0.08}V₂O₅). Reproduced with permission from Ref. [142]. Copyright (2021) Elsevier B.V.

discharge, a metastable phase $\text{Al}_x\text{V}_2\text{O}_5$ ($a = 11.468 \text{ \AA}$, $b = 3.584 \text{ \AA}$, $c = 4.372 \text{ \AA}$) is formed. The lattice parameter b increases while a and c decrease slightly compared with those of α -V₂O₅ ($a = 11.510 \text{ \AA}$, $b = 3.559 \text{ \AA}$, $c = 4.371 \text{ \AA}$). During the subsequent Al-ions insertion-extraction, a structural damage takes place and an amorphous layer is formed on the surface of α -V₂O₅ (Figure 10d), leading to the capacity decay.

Tilak et al.^[142] performed DFT calculations on the intercalation of aluminum atoms in α -V₂O₅ (Figure 10e). After placing a neutral aluminum atom in the interlayer of α -V₂O₅, valence electrons are transferred from aluminum to the V₂O₅ host along with the formation of trivalent Al-ions. After Al-ions insertion, the distance between adjacent corner-shared [VO₅] polyhedrons increases from 3.470 Å to 3.566 Å while the interlayer spacing is almost unchanged.

4. Structure Evolution of V₂O₅·nH₂O in Various Metal-Ion Batteries

4.1. Lithium-ion batteries

V₂O₅·nH₂O is favorable for lithium accommodation due to its larger interlayer spacing (~10 Å), caused by H₂O insertion, compared with that of α -V₂O₅ (~4.4 Å). The first report of V₂O₅·nH₂O for lithium storage could date back to 1983. Araki et al.^[143] reported the electrochemical intercalation of Li-ions into the interlayer of V₂O₅·1.6H₂O. During the initial Li-ions insertion, electrolyte solvent (propylene carbonate) molecules and Li-ions are co-inserted into the interlayer, resulting in the

expansion of interlayer spacing. Upon further insertion of Li-ions, the solvent is expelled by Li-ions, which results in a contraction of the interlayer spacing. The lithium diffusion coefficient (D_{Li}) in V₂O₅·1.6H₂O is estimated to be $5 \times 10^{-11} \text{ cm}^2 \text{ s}^{-1}$.^[144] The charge-discharge polarization could be reduced by combining the material with conductive additives. The typical galvanostatic charge-discharge curves of V₂O₅·nH₂O are shown in Figure 11(a). 1.6 equiv. of lithium can be stored per V₂O₅ formula unit at the end of discharge (1.5 V vs. Li⁺/Li).^[145] The shape of charge-discharge profiles is smooth during both discharge and charge processes, indicating solid-solution reaction mechanism. This is completely different with that of α -V₂O₅, which involves several phase changes during lithium intercalation (Figure 3a).

The layers of V₂O₅·nH₂O are held together by weak van der Waals force. Li-ions, water molecules, and [V₂O₅] layers undergo complex electrostatic interaction during lithium intercalation. V₂O₅·nH₂O xerogels and aerogels have distinct interlayer spacings of ~8.8 Å and ~12.7 Å, respectively, which is associated with the water number n , i.e., ~0.5 for xerogels and ~1.5 for aerogels.^[146] The structure evolution of these materials is slightly different during lithium insertion and extraction. As the XANES and XAS results shown in Figure 11(b and c), with the increase of lithium content in Li_xV₂O₅, the pre-peak intensity of vanadium edge decreases for the V₂O₅·nH₂O xerogels and increases for the aerogels.^[147] The pre-peak intensity is negatively correlated with the symmetry of [VO₆], because of the 1s–3d electronic transition. With the increase of lithium content, the symmetry of [VO₆] for V₂O₅·nH₂O xerogels is enhanced, while it is reduced for V₂O₅·nH₂O aerogels. It is also found that 6 eq. of lithium can be inserted per V₂O₅ formula unit of

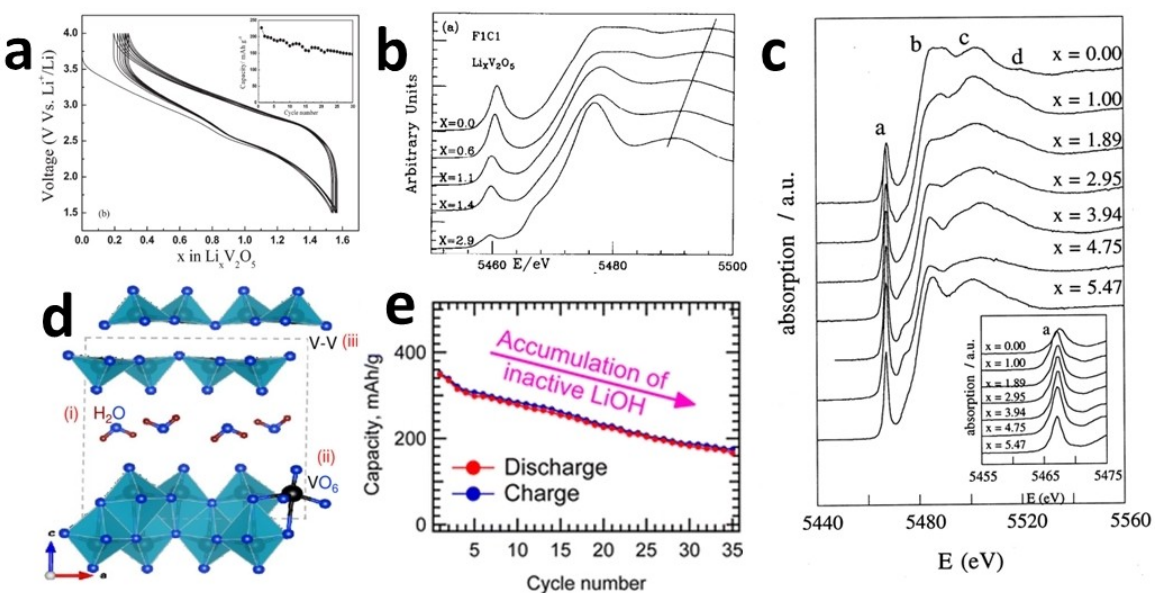


Figure 11. a) Galvanostatic cycling showing voltage-composition profile of V_2O_5 xerogel versus lithium. Reproduced with permission from Ref. [145]. Copyright (2011) American Chemical Society. b) XANES spectra for V_2O_5 xerogel with different lithium contents. Reproduced with permission from Ref. [147]. Copyright (1996) Elsevier Science B.V. c) XAS spectra of lithium intercalated V_2O_5 aerogel samples. Reproduced with permission from Ref. [146]. Copyright (1997) Elsevier Science B.V. d) The structure of $\text{V}_2\text{O}_5 \cdot 0.6\text{H}_2\text{O}$ aerogel. (e) Discharge-charge capacity as a function of cycle number for the electrochemically lithiated-delithiated $\text{V}_2\text{O}_5 \cdot 0.6\text{H}_2\text{O}$ electrodes. Reproduced with permission from Ref. [148]. Copyright (2016) American Chemical Society.

$\text{V}_2\text{O}_5 \cdot n\text{H}_2\text{O}$ aerogels, which is much higher than that of $\alpha\text{-V}_2\text{O}_5$.^[146] This may be attributed to the large number of water molecules at the interlayer, which expand the interlayer spacing and mitigate the electrostatic repulsion between Li-ions. However, the interlayer water molecules also have negative effect on the long-term cycling stability. Wangoh et al.^[148] found that lithium could react with H_2O at the interlayer space to generate LiOH . Electrochemically inactive LiOH is accumulated over each cycle (Figure 11d and e), which increases the impedance for lithium insertion and causes the capacity fading of $\text{V}_2\text{O}_5 \cdot n\text{H}_2\text{O}$.

4.2. Sodium-ion batteries

The structure evolution of $\text{V}_2\text{O}_5 \cdot n\text{H}_2\text{O}$ during sodium intercalation is similar with that of lithium intercalation. As shown in Figure 12(a), the voltage profiles of the double layered $\text{V}_2\text{O}_5 \cdot n\text{H}_2\text{O}$ are also smooth, which are significantly different with those of $\alpha\text{-V}_2\text{O}_5$ and imply the solid-solution reaction mechanism.^[149] Note that the double layered V_2O_5 tested in Figure 12(a) is achieved by annealing hydrous V_2O_5 in vacuum at 120 °C. Under this temperature, the water molecules in the interlayers cannot be completely removed.^[150,151] The double layered $\text{V}_2\text{O}_5 \cdot n\text{H}_2\text{O}$ exhibits a higher output voltage at 3 V (vs. Na^+/Na) than that of $\alpha\text{-V}_2\text{O}_5$.

According to the XAS and XRD results reported by Tepavcevic and co-workers (Figure 12b and c), the structure evolution of $\text{V}_2\text{O}_5 \cdot n\text{H}_2\text{O}$ mainly involves the variation of layer spacing during the sodium insertion-extraction.^[149] At the end of sodium insertion (1.5 V vs. Na^+/Na), the interlayer spacing of

$\text{V}_2\text{O}_5 \cdot n\text{H}_2\text{O}$ increases from 13.5 Å to 16.1 Å and a reversible capacity of 250 mAh g⁻¹ can be achieved, which is corresponding to 2 equiv. of Na-ions inserted per V_2O_5 formula unit. Both the long- and short-range order is maintained during the sodium insertion. After sodium extraction, although the double layered structure of V_2O_5 is restored, the long-range order is lost while short-range order is preserved.

The interlayer spacing of the double layered V_2O_5 can be adjusted by intercalating water molecules or organic molecules.^[152] Recently, Tang et al.^[153] introduces *m*-benzoquinone (*m*-BQ) into V_2O_5 forming (*m*-BQ)_{0.15} $\text{V}_2\text{O}_5 \cdot 0.5\text{H}_2\text{O}$ ((*m*-BQ)-VO). The interlayer spacing expands from 11.5 Å for $\text{V}_2\text{O}_5 \cdot \text{H}_2\text{O}$ to 13.7 Å for (*m*-BQ)-VO. As shown by the galvanostatic charge-discharge curves in Figure 12(d), (*m*-BQ)-VO displays a discharge (sodiation) plateau at ~1.7 V (vs. Na^+/Na), suggesting a two-phase sodium storage process. The average working voltage of (*m*-BQ)-VO is lower than that of $\text{V}_2\text{O}_5 \cdot n\text{H}_2\text{O}$ (Figure 12a), which may be associated with the slow kinetics of sodium insertion caused by the hindrance from the large *m*-BQ molecules. First principle calculations indicate that the inserted sodium is coordinated by three oxygen atoms from three different *m*-BQ molecules (Figure 12e and f), which results in a low formation energy of -3.86 eV. As a result, these Na-ions cannot be extracted during the charge process, leading to irreversible capacity loss of the material.

4.3. Potassium-ion batteries

$\text{V}_2\text{O}_5 \cdot n\text{H}_2\text{O}$ exhibits better compatibility with potassium compared with $\alpha\text{-V}_2\text{O}_5$.^[154] As shown in Figure 13(a), $\text{V}_2\text{O}_5 \cdot 0.6\text{H}_2\text{O}$

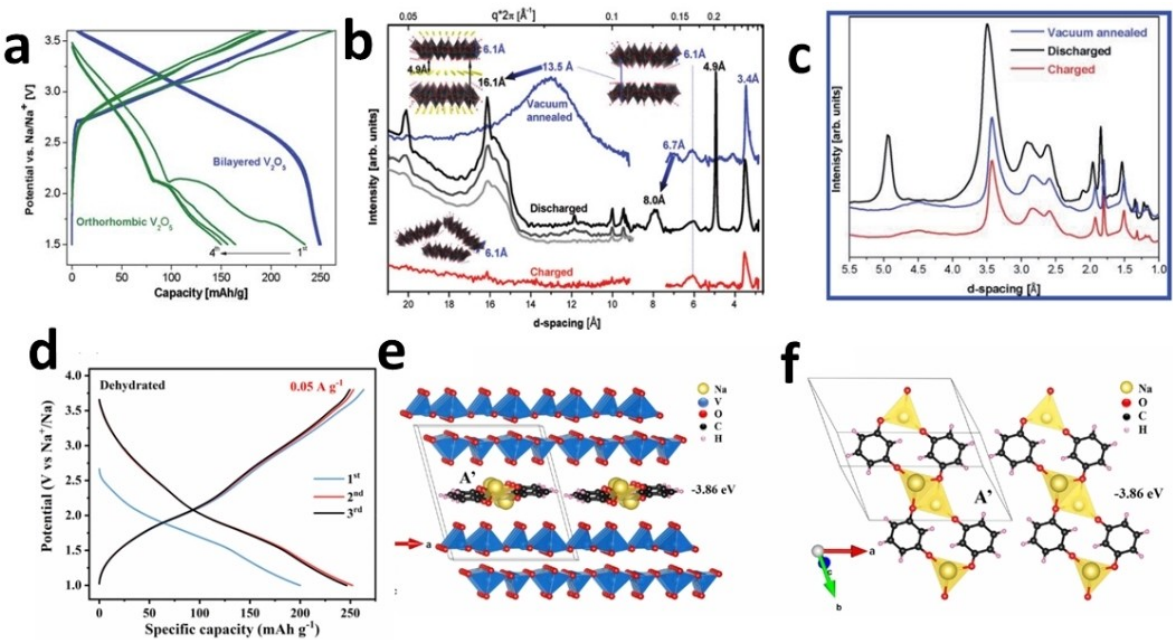


Figure 12. a) First four charge-discharge cycles of bilayered V_2O_5 and orthorhombic V_2O_5 electrodes. b) Small and wide angle X-ray scattering spectra for bilayered V_2O_5 : electrochemically deposited double layered V_2O_5 (blue); after discharging with the current of $630 \mu\text{A}$ (black), $120 \mu\text{A}$ (gray), $20 \mu\text{A}$ (light gray), and after cycling at $120 \mu\text{A}$ in the charge state (red). c) Synchrotron XRD spectra of the bilayered V_2O_5 annealed in vacuum at 120°C (blue). Reproduced with permission from Ref. [149]. Copyright (2011) American Chemical Society. d) The first three galvanostatic charge-discharge curves of $(m\text{-BQ})_{0.15}V_2O_5 \cdot 0.5H_2O$ at 0.05 A g^{-1} . e and f) The site of Na-ions intercalated in $(m\text{-BQ})_{0.15}V_2O_5 \cdot 0.5H_2O$. Reproduced with permission from Ref. [153]. Copyright (2022) Elsevier B.V.

could provide a high discharge (potassiation) capacity of $\sim 224.4 \text{ mAh g}^{-1}$ at 50 mA g^{-1} , corresponding to ~ 1.7 equiv. of potassium inserted per V_2O_5 formula unit. During potassium insertion, the interlayer spacing shrinks, which is attributed to the electrostatic interaction between potassium and oxygen. At the end of potassium extraction, the structure of $V_2O_5 \cdot 0.6H_2O$ is restored without new phase formed (Figure 13b). However, the working voltage of $V_2O_5 \cdot 0.6H_2O$ in KIBs is lower than that in LIBs and NIBs. This may be due to the steric effect between large K-ions and water molecules. Recent research suggests a dual-mode mechanism for potassium storage in $V_2O_5 \cdot 1.8H_2O$, including both surface pseudocapacitive effect and bulk diffusion-limited intercalation.^[155]

Besides electrochemical approaches, potassium can also be inserted into the interlayer of hydrated V_2O_5 by wet chemical method.^[156,157] Clites et al.^[157] firstly reported the application of potassium pre-intercalated $V_2O_5 \cdot nH_2O$, $K_{0.42}V_2O_5 \cdot 0.25H_2O$, as a cathode material for non-aqueous KIBs (Figure 13c and d). The potassium pre-intercalated material has a d spacing of 9.62 \AA . K-ions and water molecules are located between the large interlayers while their precise positions are not available. As shown in Figure 13(c), the charge-discharge curves display several small plateaus. During the first charge (depotassiation) process, ~ 0.38 equiv. of potassium could be extracted per V_2O_5 formula unit, corresponding to a charge specific capacity of 54 mAh g^{-1} . Water molecules and the remaining potassium in the interlayer serve as pillars to stabilize the double layered structure. In the subsequent potassium insertion process, a high discharge capacity of 268 mAh g^{-1} can be achieved, corresponding to insertion of 1.89 eq. of potassium per V_2O_5 formula unit,

and the interlayer spacing increases because of the enhanced electrostatic repulsion between layers.^[156]

Our group explored the role of water molecules on the potassium extraction-insertion mechanism of $K_{0.5}V_2O_5 \cdot 0.5H_2O$ through experimental methods and theoretical calculations (Figure 13e).^[158] $K_{0.5}V_2O_5 \cdot 0.5H_2O$ exhibits capacity retention of 81.1% after 200 cycles, while the anhydrous counterpart only maintains 33.3% of its initial capacity after 100 cycles. Two phases, namely δ_1 - and δ_2 -phase, co-exist during potassium insertion into $K_{0.5}V_2O_5$, which cause multistep phase transition and result in the large volume change of the material, leading to the capacity loss. In contrast, $K_{0.5}V_2O_5 \cdot 0.5H_2O$ undergoes a single-phase solid-solution reaction during potassiation-depotassiation process and experiences a relatively smaller volume variation. The interlayer water molecules act as pillars to mitigate the volume variations for $K_{0.5}V_2O_5 \cdot 0.5H_2O$, contributing to the stabilization of the material during charge-discharge.

4.4. Magnesium-ion batteries

The reaction kinetics for magnesium insertion into the single layered $\alpha\text{-}V_2O_5$ is slow due to the narrow interlayer spacing of $\alpha\text{-}V_2O_5$ and the multivalent nature of Mg-ions. As a result, the electrochemical insertion of Mg-ions into $\alpha\text{-}V_2O_5$ is difficult at room temperature. However, the magnesium storage behavior of $V_2O_5 \cdot nH_2O$ is significantly different. As shown in Figure 14(a), at the end of magnesium insertion (1.4 V vs. Mg^{2+}/Mg), a discharge capacity of 114 mAh g^{-1} is achieved at room temperature, which corresponds to 0.35 equiv. of magnesium stored

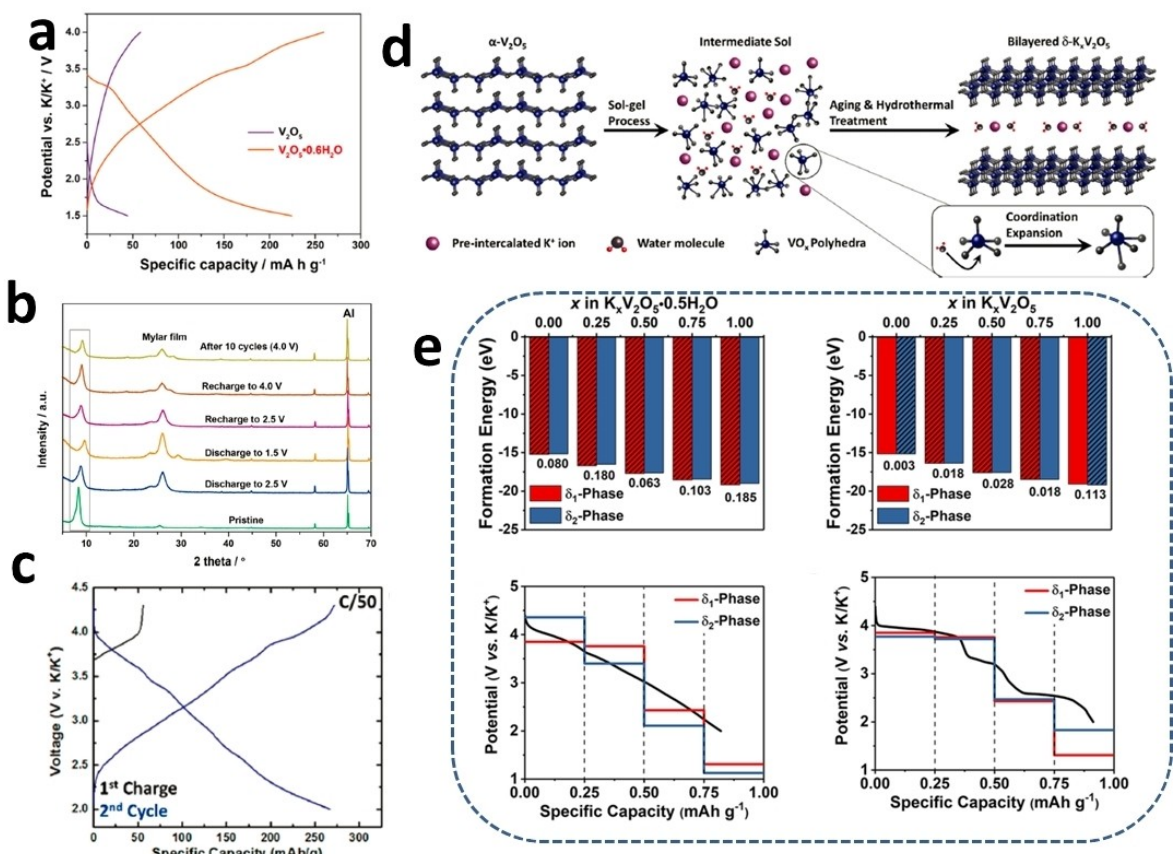


Figure 13. a) Initial galvanostatic discharge and charge cycles of $\text{V}_2\text{O}_5 \cdot 0.6\text{H}_2\text{O}$ and $\alpha\text{-V}_2\text{O}_5$ electrodes at current density of 50 mA g⁻¹ in the voltage range of 1.5–4.0 V (vs. K^+/K). b) Ex situ XRD patterns of the pristine $\text{V}_2\text{O}_5 \cdot 0.6\text{H}_2\text{O}$ electrode, $\text{V}_2\text{O}_5 \cdot 0.6\text{H}_2\text{O}$ electrodes discharged to 2.5 V (vs. K^+/K) and 1.5 V (vs. K^+/K), recharged to 2.5 V (vs. K^+/K) and 4.0 V (vs. K^+/K), and after 10 full discharge/charge cycles. Reproduced with permission from Ref. [181]. Copyright (2017) American Chemical Society. c) Electrochemical characterization of $\delta\text{-K}_{0.42}\text{V}_2\text{O}_5 \cdot 0.25\text{H}_2\text{O}$ at a current rate of C/50 (~6 mA g⁻¹). d) Schematic illustration of the chemical pre-intercalation of $\delta\text{-K}_{0.42}\text{V}_2\text{O}_5 \cdot 0.25\text{H}_2\text{O}$. Reproduced with permission from Ref. [157]. Copyright (2018) American Chemical Society. e) Formation energies and calculated voltages of $\text{K}_x\text{V}_2\text{O}_5 \cdot 0.5\text{H}_2\text{O}$ and $\text{K}_x\text{V}_2\text{O}_5$. Reproduced with permission from Ref. [158]. Copyright (2021) The Royal Society of Chemistry.

per V_2O_5 formula unit. Sa et al.^[159] unveiled the detailed structural evolution of $\text{V}_2\text{O}_5 \cdot n\text{H}_2\text{O}$ ($n = 0.6$) xerogels. As shown in Figure 14(b), at the end of magnesium insertion, the interlayer distance of $\text{V}_2\text{O}_5 \cdot 0.6\text{H}_2\text{O}$ is 10.9 Å due to the strong electrostatic attraction between inserted Mg-ions and the V_2O_5 host. After the extraction of all Mg-ions, the interlayer spacing is enlarged to 12.8 Å.

Interestingly, solvent molecules, such as diglyme and water, could co-intercalate with Mg-ions because of the strong solvation effect of Mg-ions.^[160] Taking water as an example, it could reduce the electrostatic repulsion between Mg-ions in the interlayers. The structures of fully magnesiated and demagnesiated V_2O_5 xerogels are shown in Figure 14(c). In the fully magnesiated phase, H₂O molecules and Mg-ions are located between the interlayers of $\text{V}_2\text{O}_5 \cdot n\text{H}_2\text{O}$. Magnesium is 6-fold coordinated with oxygen atoms in which two belong to the V_2O_5 host and four are from the H₂O molecules.^[161] Upon magnesium removal, the hydrogen bonding among the water molecules becomes more prominent. Two kinds of stable hydrogen bond are arranged along the *a* and *c* directions, respectively. One is ascribed to hydrogen and oxygen of the next-nearest water while the other belongs to hydrogen and

lattice oxygen. The O–H distance for the former hydrogen bond is 1.6–1.8 Å while it is 2.2–2.6 Å for the latter one.

Gautam et al.^[161] investigated the role of H₂O during Mg-ions intercalation in $\text{V}_2\text{O}_5 \cdot n\text{H}_2\text{O}$ xerogels. Whether water co-intercalation with Mg-ions or not depends on the water activity in the electrolyte. According to the minimized grand-potential at 0 K (Figure 14d), the stable Mg-xerogel V_2O_5 phases are function of water activity $a_{\text{H}_2\text{O}}$ and the Mg chemical potential (μ_{Mg}). Such as $\mu_{\text{Mg}} = 0$ and using wet electrolyte (water activity $a_{\text{H}_2\text{O}} = \sim 1$), H₂O molecules coordinating with Mg-ions shuttle into the interlayer space of $\text{V}_2\text{O}_5 \cdot n\text{H}_2\text{O}$ xerogels to form $\text{Mg}_x\text{V}_2\text{O}_5 \cdot \text{H}_2\text{O}$ ($0 \leq x \leq 0.5$). Using dry electrolyte, $10^{-6} < a_{\text{H}_2\text{O}} < 10^{-2}$, H₂O co-intercalation occurs under the low magnesium content condition ($0 \leq x \leq 0.25$) with the formation of $\text{Mg}_x\text{V}_2\text{O}_5 \cdot 0.5\text{H}_2\text{O}$. Using super dry electrolyte ($a_{\text{H}_2\text{O}} < 10^{-7}$), no water molecule exists in the interlayer space and $\text{Mg}_x\text{V}_2\text{O}_5$ ($0 \leq x \leq 0.5$) is formed.

Pre-magnesiated $\text{V}_2\text{O}_5 \cdot n\text{H}_2\text{O}$ has also been reported as electrode materials for MIBs because of the enhanced physicochemical properties. As shown in Figure 14(e), $\text{Mg}_{0.3}\text{V}_2\text{O}_5 \cdot 1.1\text{H}_2\text{O}$ with an interlayer spacing of 11.9 Å has an enhanced electrical conductivity of $8.5 \times 10^2 \text{ S m}^{-1}$ compared

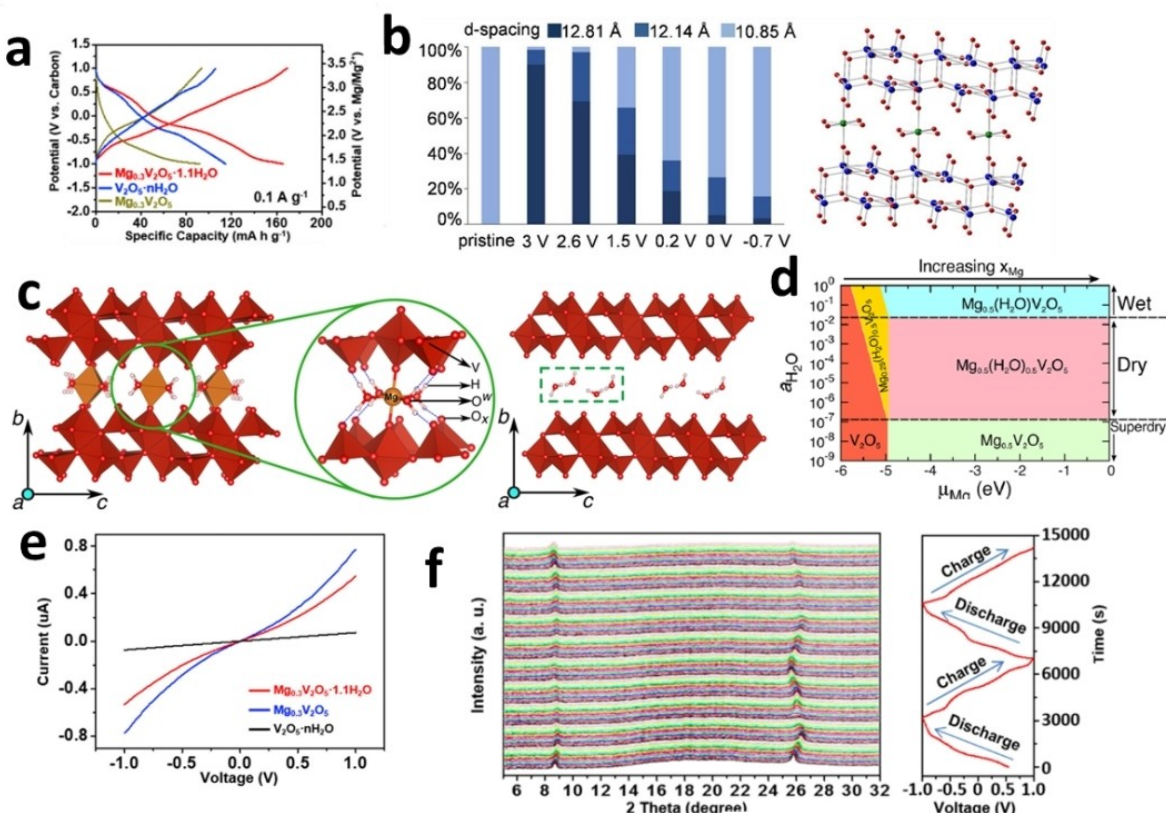


Figure 14. a) Charge-discharge curves of $\text{Mg}_{0.3}\text{V}_2\text{O}_5 \cdot 1.1\text{H}_2\text{O}$, $\text{V}_2\text{O}_5 \cdot n\text{H}_2\text{O}$, and $\text{Mg}_{0.3}\text{V}_2\text{O}_5$. Reproduced with permission from Ref. [162]. Copyright (2019) Elsevier Inc. b) The distribution of interlayer spacing for $\text{V}_2\text{O}_5 \cdot n\text{H}_2\text{O}$ xerogels at different potentials and the structure of $\text{Mg}_{0.25}\text{V}_2\text{O}_5 \cdot n\text{H}_2\text{O}$ with a layer spacing of $\sim 10.9 \text{ \AA}$. Green, blue, and red balls stand for magnesium, vanadium, and oxygen, respectively. Reproduced with permission from Ref. [159]. Copyright (2016) American Chemical Society. c) Structures of the fully magnesiated ($x_{\text{Mg}} = 0.5$) and demagnesiated xerogels with one H_2O per V_2O_5 formula unit. d) Grand-potential phase diagram at 0 K of Mg-xerogel V_2O_5 as a function of various electrolytic conditions and Mg chemical potentials. Reproduced with permission from Ref. [161]. Copyright (2016) American Chemical Society. e) I - V curves of $\text{V}_2\text{O}_5 \cdot n\text{H}_2\text{O}$, $\text{Mg}_{0.3}\text{V}_2\text{O}_5 \cdot 1.1\text{H}_2\text{O}$, and $\text{Mg}_{0.3}\text{V}_2\text{O}_5$. f) *In situ* XRD measurement of $\text{Mg}_{0.3}\text{V}_2\text{O}_5 \cdot 1.1\text{H}_2\text{O}$ during the first two electrochemical cycles. Reproduced with permission from Ref. [162]. Copyright (2019) Elsevier Inc.

with that of $\text{V}_2\text{O}_5 \cdot n\text{H}_2\text{O}$ (10.1 S m^{-1}).^[162] Mg-ions coordinate with six oxygen atoms of the host structure in the form of $[\text{MgO}_6]$ octahedrons. Water molecules are arranged in the a - b plane by stable hydrogen bond, which is similar to Sa's results.^[159] The structure evolution of $\text{Mg}_{0.3}\text{V}_2\text{O}_5 \cdot 1.1\text{H}_2\text{O}$ during magnesium insertion-extraction just involves the variation of interlayer spacing. During the magnesiation process, the interlayer spacing is reduced from 11.9 \AA to 11.4 \AA . The subsequent demagnesiation process results in the structure recovery of $\text{Mg}_{0.3}\text{V}_2\text{O}_5 \cdot 1.1\text{H}_2\text{O}$ without the extraction of pre-intercalated magnesium (Figure 14f).

4.5. Zinc-ion batteries

The structure evolution of $\text{V}_2\text{O}_5 \cdot n\text{H}_2\text{O}$ during Zn-ions insertion-extraction is mainly related to the expansion and contraction of the interlayer spacing, which is similar with that of magnesium accommodation. The water number n of $\text{V}_2\text{O}_5 \cdot n\text{H}_2\text{O}$ plays a determining role in its cycling performance. Li *et al.*^[163] prepared a series of $\text{V}_2\text{O}_5 \cdot n\text{H}_2\text{O}$ samples with different water contents by heat-treating the as-prepared $\text{V}_2\text{O}_5 \cdot 1.6\text{H}_2\text{O}$ at 100, 150, 200,

300, and 400°C . The water number n decreases in turn with the rising of temperature. $\text{V}_2\text{O}_5 \cdot 1.6\text{H}_2\text{O}$ is transformed into $\alpha\text{-V}_2\text{O}_5$ (anhydrous phase) after being treated at the temperature higher than 340°C . The hydrous phase, treated at 150°C , displays the best cycling stability and a discharge (zinc intercalation) capacity of 179 mAh g^{-1} is achieved after 600 cycles at 0.5 A g^{-1} .

The role of water molecules in $\text{V}_2\text{O}_5 \cdot n\text{H}_2\text{O}$ was also revealed by Yan and co-workers.^[164] $\text{V}_2\text{O}_5 \cdot n\text{H}_2\text{O}$ is composed with graphene as $\text{V}_2\text{O}_5 \cdot n\text{H}_2\text{O}/\text{graphene}$ (VOG) to improve its conductivity. About 1.29 equiv. of structural water is placed in per VOG unit with an interlayer spacing of 12.6 \AA . As shown in Figure 15(a), the charge-discharge curves of VOG have two distinct slopes, corresponding to two solid-solution reactions. It delivers an initial discharge (zinc intercalation) capacity of 381 mAh g^{-1} , indicating that about 1.5 equiv. of Zn-ions could be accommodated per V_2O_5 formula unit. Regarding the cycling performance, it exhibits 71% retention of the maximum capacity after 900 cycles (Figure 15b). However, the anhydrous counterpart, obtained after heating VOG at 350°C (VOG-350), provides a relatively low capacity and poor cycling stability.

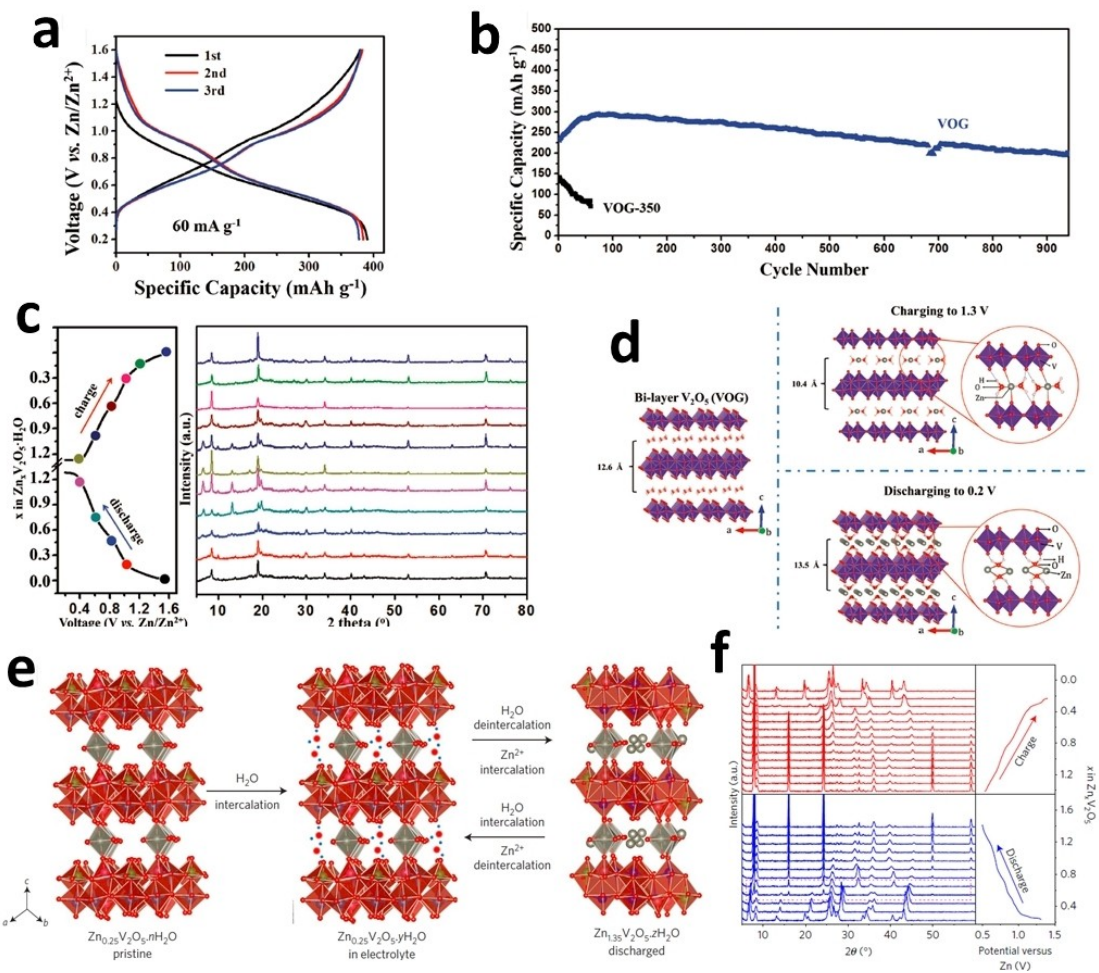


Figure 15. a) Charge-discharge curves for the first three cycles of the as-prepared VOG. b) Cycling performance of VOG and VOG-350 at 6 Ag^{-1} . c) XRD study of VOG at different charge and discharge states. d) The proposed crystal structures of pristine VOG, VOG after charging to 1.3 V (vs. Zn^{2+}/Zn), and discharging to 0.2 V (vs. Zn^{2+}/Zn). Reproduced with permission from Ref. [164]. Copyright (2017) WILEY-VCH Verlag GmbH & Co. KGaA, Weinheim. e) Scheme showing reversible water intercalation into $\text{Zn}_{0.25}\text{V}_2\text{O}_5 \cdot n\text{H}_2\text{O}$ immersed in 1 M ZnSO_4 aqueous electrolyte. f) Operando XRD study of the $\text{Zn}_{0.25}\text{V}_2\text{O}_5$ electrode during cycling. Reproduced with permission from Ref. [170]. Copyright Macmillan Publishers Limited, part of Springer Nature.

The interlayer spacing of VOG is increased to 13.5 Å after Zn-ions intercalation at 0.2 V (vs. Zn^{2+}/Zn). 1.2 mol Zn-ions are incorporated into V_2O_5 with the co-intercalation of water molecules and CF_3SO_3^- anions in the electrolyte.^[165,166] After Zn-ions extraction at 1.3 V (vs. Zn^{2+}/Zn), the interlayer spacing is decreased to 10.4 Å (Figure 15c) which is attributed to the formation of complex bonds among Zn^{2+} , CF_3SO_3^- , H_2O , and lattice oxygen. The water number n increases to 1.8. The enhanced electrochemical performance of VOG is attributed to the structural water which shields the charge of Zn-ions and stabilizes the host structure by reducing the electrostatic interaction between Zn-ions and V_2O_5 (Figure 15d).^[167]

Pre-intercalated $\text{V}_2\text{O}_5 \cdot n\text{H}_2\text{O}$ has also been reported as electrode materials for ZIBs due to its expanded interlayer spacing and enhanced conductivity.^[168,169] Linda et al.^[170] investigated the structure evolution of zinc pre-inserted $\text{Zn}_{0.25}\text{V}_2\text{O}_5 \cdot n\text{H}_2\text{O}$ during the Zn-ions insertion-extraction. $\text{Zn}_{0.25}\text{V}_2\text{O}_5 \cdot n\text{H}_2\text{O}$ has a double layered structure with triclinic symmetry and space group P . The interlayer spacing is determined to be 10.8 Å with ~0.85 equiv. of structural water

located at the $a-b$ plane per V_2O_5 unit (Figure 15e). Zn-ions are located between the interlayers and act as pillars with the $[\text{ZnO}_6]$ octahedron coordination. The presence of Zn-ions stabilizes the layered structure during Zn-ions insertion/extraction and enhances the structure stability. Upon immersion in the aqueous electrolyte, the interlayer spacing is increased from 10.8 Å to 12.9 Å caused by the water intercalation. Subsequent drying causes the interlayer spacing to reversibly shrink to pristine state, indicating the excellent structure reversibility of the sample. A high capacity of 282 mAh g^{-1} is obtained at the end of zinc intercalation, corresponding to 1.1 equiv. of Zn-ions inserted per $\text{Zn}_{0.25}\text{V}_2\text{O}_5 \cdot n\text{H}_2\text{O}$ formula unit. The insertion of Zn-ions expels water out of the interlayer space, while water molecules are re-inserted into the interlayer during Zn-ions extraction. $\text{Zn}_x\text{V}_2\text{O}_5 \cdot n\text{H}_2\text{O}$ experiences two solid-solution reactions which are separated by a phase transition at $x = 0.55$ (Figure 15f). In the regime $0.25 < x < 0.55$, the interlayer spacing undergoes a small contraction. The phase transition takes place in the regime $0.55 < x < 0.6$, and the interlayer distance is decreased from 12.3 Å to 11.0 Å, which is similar

with that of the pristine state and attributed to the expulsion of water from the structure. In the regime $0.55 < x < 1.4$, the d -spacing is constant. However, the structure continues to evolve with the increasing of zinc content caused by the different proportion of zinc ions/vacancy.^[171] The zinc extraction process for $Zn_xV_2O_5 \cdot nH_2O$ follows the reverse evolution of zinc insertion.

4.6. Calcium-ion batteries

$V_2O_5 \cdot nH_2O$ possesses a larger interlayer spacing than $\alpha\text{-}V_2O_5$, which is in favor of the storage of Ca-ions. S. Chae et al.^[172] reported the structure evolution of $V_2O_5 \cdot 0.63H_2O$ during Ca-ions insertion-extraction. 1 M $Ca(NO_3)_2$ aqueous solution was used as the electrolyte and the testing voltage was in the range of -0.45 V to 0.76 V (vs. Ag/AgCl). As shown in Figure 16(a), $V_2O_5 \cdot 0.63H_2O$ delivers an initial discharge (calcium intercalation) capacity of 203 mAh g $^{-1}$ with an average discharge voltage of 2.76 V (vs. Ca^{2+}/Ca) at 0.1 C (13.88 mA g $^{-1}$). 1.08 equiv. of Ca-ions could be accommodated per V_2O_5 formula unit. The discharged product is expressed as $Ca_{1.08}V_2O_5 \cdot 1.15H_2O$ with an interlayer spacing of 12.53 Å (Figure 16b). Water molecules are co-inserted into the interlayer space of $V_2O_5 \cdot 0.63H_2O$. During the subsequent charge (calcium extraction) process, 0.72 equiv. of Ca-ions could be extracted per V_2O_5 formula unit and the charged product is expressed as $Ca_{0.36}V_2O_5 \cdot 1.08H_2O$ with an interlayer spacing of 11.52 Å. Water molecules are co-extracted out of the V_2O_5 host structure. This may be attributed to the electrostatic interaction between Ca-ions and water molecules. 0.36 eq. of Ca-ions per V_2O_5 formula unit remains after recharging. The authors hypothesized that this may be attributed to the spontaneous insertion of Ca-ions from the aqueous electrolyte to $V_2O_5 \cdot 0.63H_2O$.

Xu et al.^[173] explored magnesium pre-inserted $V_2O_5 \cdot nH_2O$, $Mg_{0.25}V_2O_5 \cdot H_2O$, as a cathode material for CIBs. It has an interlayer spacing of 10.76 Å. Mg-ions and water molecules are located between the interlayers in the form of $Mg^{2+}[4H_2O]$ (Figure 16c). Due to the strong screening effect of H_2O and the large interlayer spacing, 0.36 eq. of Ca-ions per V_2O_5 formula unit can be reversibly inserted and extracted, corresponding to a reversible capacity of ~ 93.7 mAh g $^{-1}$. The interlayer spacing is only changed by 0.09 Å during calcium insertion-extraction. The DFT calculation and ICP results reveal that the binding strength between Mg-ions and water molecules is stronger than that between Ca-ions and water molecules (Figure 16d). Mg-ions will not be brought out during Ca-ions insertion-extraction and play a crucial role for stabilizing the layered structure.

The structure evolution of calcium pre-intercalated $V_2O_5 \cdot nH_2O$ as electrode materials for CIBs is complex. Jeon et al.^[174] proposed a “stacking-faulted model” to describe the structure evolution of $Ca_{0.28}V_2O_5 \cdot H_2O$ during the calcium extraction-insertion. $Ca_{0.28}V_2O_5 \cdot H_2O$ has an interlayer spacing of 10.8 Å with water molecules bonding with Ca-ions disorderly. As shown in Figure 17(a), at the end of first calcium extraction, the XRD pattern indicates that the (001) peak shifts toward lower angle and the (00l) peaks appear, indicating that a two-fold superstructure may be formed. The detailed structure and X-ray Rietveld refinement profile are shown in Figure 17(b and c). At the end of the first calcium insertion, an amorphous-like phase is generated which is caused by a large amount of calcium placed at the interlayers. However, the material again becomes highly crystalline during the following calcium extraction. A “stacking-faulted model” is then used to explain this phenomenon (Figure 17d). In the original structure, Ca-ions and water molecules reside in every interlayer. After the first calcium extraction, Ca-ions and water in every two interlayers are

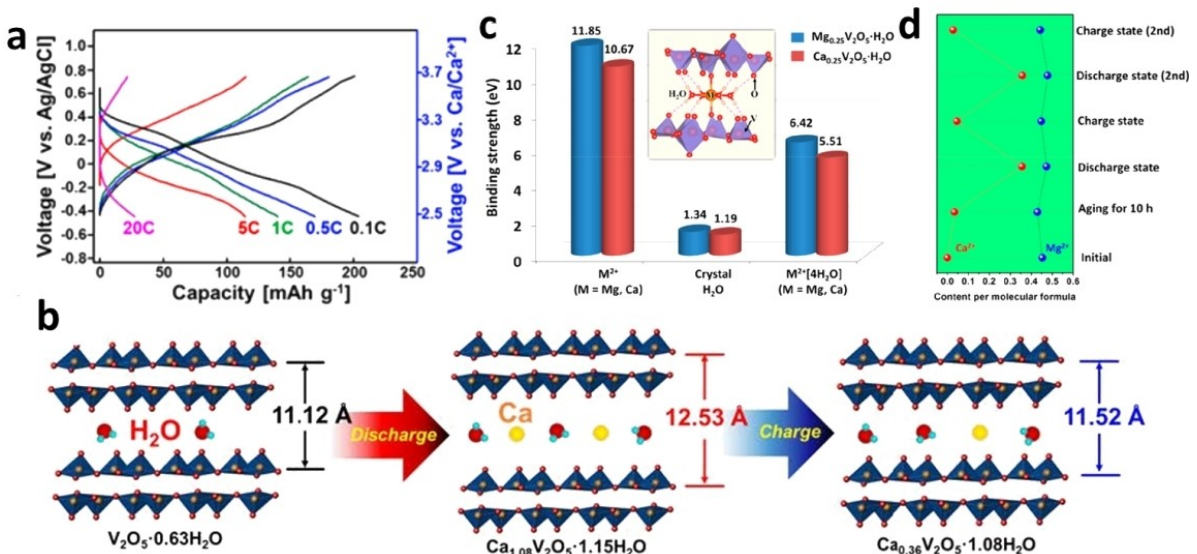


Figure 16. a) Galvanostatic discharge-charge curves of $V_2O_5 \cdot 0.63H_2O$ in CIBs. b) A conceptual illustration of the evolution of the $V_2O_5 \cdot 0.63H_2O$ structure upon cycling. Reproduced with permission from Ref. [172]. Copyright (2020) Wiley-VCH Verlag GmbH & Co. KGaA, Weinheim. c) Calculated binding strengths of M^{2+} ($M = Mg, Ca$), crystal H_2O , and $M^{2+}[4H_2O]$ in the crystal of $M_{0.25}V_2O_5 \cdot H_2O$. d) Content variation of Mg-ions and Ca-ions per molecular formula of $Mg_{0.25}V_2O_5 \cdot H_2O$ at different charge/discharge states. Reproduced with permission from Ref. [173]. Copyright (2019) American Chemical Society.

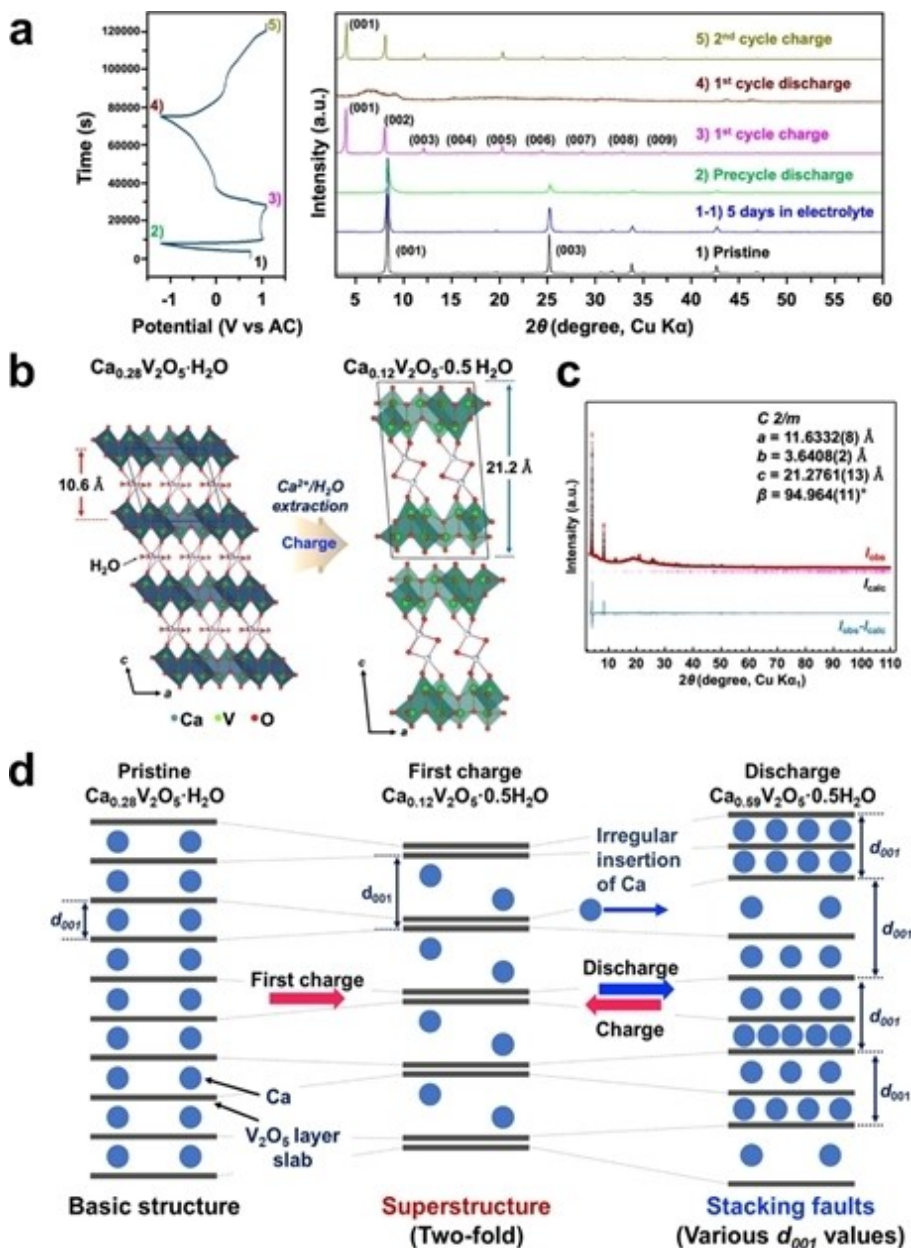


Figure 17. a) XRD patterns of $\text{Ca}_{0.28}\text{V}_2\text{O}_5 \cdot \text{H}_2\text{O}$ measured at each stage of galvanostatic charge – discharge process. b) Comparison of the pristine ($\text{Ca}_{0.28}\text{V}_2\text{O}_5 \cdot \text{H}_2\text{O}$) and charged ($\text{Ca}_{0.12}\text{V}_2\text{O}_5 \cdot 0.5\text{H}_2\text{O}$) structures. c) X-ray Rietveld refinement profile of $\text{Ca}_{0.12}\text{V}_2\text{O}_5 \cdot 0.5\text{H}_2\text{O}$ (red circle: experimental data; black line: calculated data; blue line: difference; and pink bars: Bragg positions). d) Schematic illustration of the charge-discharge mechanism during cycling, where the stacking-faulted model is a conceptually illustrating model that further in-depth investigation should confirm. Reproduced with permission from Ref. [174]. Copyright (2022) American Chemical Society.

completely removed, which doubles the lattice parameter c (Figure 17c). During the calcium insertion, Ca-ions are inserted into the occupied and empty interlayers irregularly, which results in the “stacking faults” of V_2O_5 layers and the amorphous characteristics of the XRD pattern.

4.7. Aluminum-ion batteries

The accommodation of aluminum for $\text{V}_2\text{O}_5 \cdot 0.4\text{H}_2\text{O}$ was verified by Le and co-workers in 1998.^[175] The interlayer spacing of

$\text{V}_2\text{O}_5 \cdot 0.4\text{H}_2\text{O}$ was 12.5 \AA caused by the presence of acetone residue. $0.1 \text{ M Al}(\text{CF}_3\text{SO}_3)_3$ in propylene carbonate was used as the electrolyte. $\text{V}_2\text{O}_5 \cdot 0.4\text{H}_2\text{O}$ was tested using a two-electrode configuration with $\text{Al}_{1.33}\text{V}_2\text{O}_5$ as the counter electrode. At the end of the first aluminum insertion, 0.81 equiv. of Al-ion per V_2O_5 formula unit is inserted forming $\text{Al}_{0.81}\text{V}_2\text{O}_5$. At the end of the first aluminum extraction, $\text{Al}_{0.81}\text{V}_2\text{O}_5$ is transformed into $\text{Al}_{0.25}\text{V}_2\text{O}_5$. This may be attributed to the strong bonding between Al-ions and oxygen of the host structure.^[142] During the subsequent charge-discharge cycles, 0.29 equiv. of Al-ions

could be reversibly inserted and extracted per V_2O_5 formula unit, corresponding to a specific energy of 750 Wh kg^{-1} .

Diem et al.^[176] studied the sites of Al-ions stored in $V_2O_5 \cdot 1.15H_2O$. $V_2O_5 \cdot 1.15H_2O$ has an interlayer spacing of 9.84 \AA . 1-ethyl-3-methylimidazolium chloride ([EMIM]Cl) mixed with aluminum chloride ($AlCl_3$) in the ratio of 1:1.5 was used as the electrolyte. As the CV curve shown in Figure 18(a), in the voltage range of 0.02–2.5 V (vs. Al^{3+}/Al), there are two pairs of cathodic/anodic peaks at 0.64/0.80 V (vs. Al^{3+}/Al) and 0.78/0.94 V (vs. Al^{3+}/Al), which are corresponding to two different Al-ions intercalation sites.^[177] At the high potential, Al-ions are firstly placed at site-a, which is close to the oxygen atoms of the square planar (Figure 18b). At the low potential, Al-ions are further stored at site-b which is close to the apical oxygen atom of the polyhedrons. It was further found that when copper foil was used both as the current collector and the cathode material, Cu-ions could be dissolved in the electrolyte and doped into the interlayer space of V_2O_5 forming $Cu_xV_2O_5$ bronze (Figure 18c). During the following aluminum insertion-extraction process, the structural integrity of V_2O_5 is preserved, which is enabled by the copper doping. The electrical conductivity of the $V_2O_5 \cdot 1.15H_2O$ increases from $0.16 \times 10^{-6} \text{ S cm}^{-1}$ to $0.16 \times 10^{-2} \text{ S cm}^{-1}$ after the copper doping. This demonstrates that heteroatomic doping may be a feasible solution for developing high-performance materials for AlBs.

5. Summary and Outlook

In summary, we have briefly reviewed the structure evolution of single layered α - V_2O_5 and double layered $V_2O_5 \cdot nH_2O$ for their applications as electrode materials in various metal-ion batteries, including LIBs, NIBs, KIBs, MIBs, ZIBs, ClIBs, and AlIBs. The interlayer spacing, cost, safety, theoretical capacity, and thermal stability of α - V_2O_5 and $V_2O_5 \cdot nH_2O$ are compared in the radar plot shown in Figure 19. Due to the different sizes and valence states of these metal-ions, α - V_2O_5 and $V_2O_5 \cdot nH_2O$ experience quite distinct structure evolution in these batteries.

α - V_2O_5 is stacked by the $[V_2O_5]$ layers consisting of edge- and corner-shared $[VO_5]$ polyhedrons, which has a narrow *d*-spacing of $\sim 4.4 \text{ \AA}$ and possesses high structural flexibility during various metal-ions intercalation. For small and monovalent Li-ions, α - V_2O_5 undergoes a series of reversible phase transitions, namely $\alpha \rightarrow \epsilon \rightarrow \delta \rightarrow \gamma \rightarrow \omega$, with the $[V_2O_5]$ layers seriously puckered. For large monovalent Na- and K-ions, the insertion resistance is significantly increased and irreversible phases usually take place during ions insertion-extraction. Multivalent Mg-, Zn-, Ca-, and Al-ions exert strong electrostatic interaction with α - V_2O_5 , which leads to high diffusion barriers and slow intercalation kinetics.

Regarding $V_2O_5 \cdot nH_2O$ which is formed by edge- and corner-shared $[VO_6]$ octahedrons, it always exists in the form of

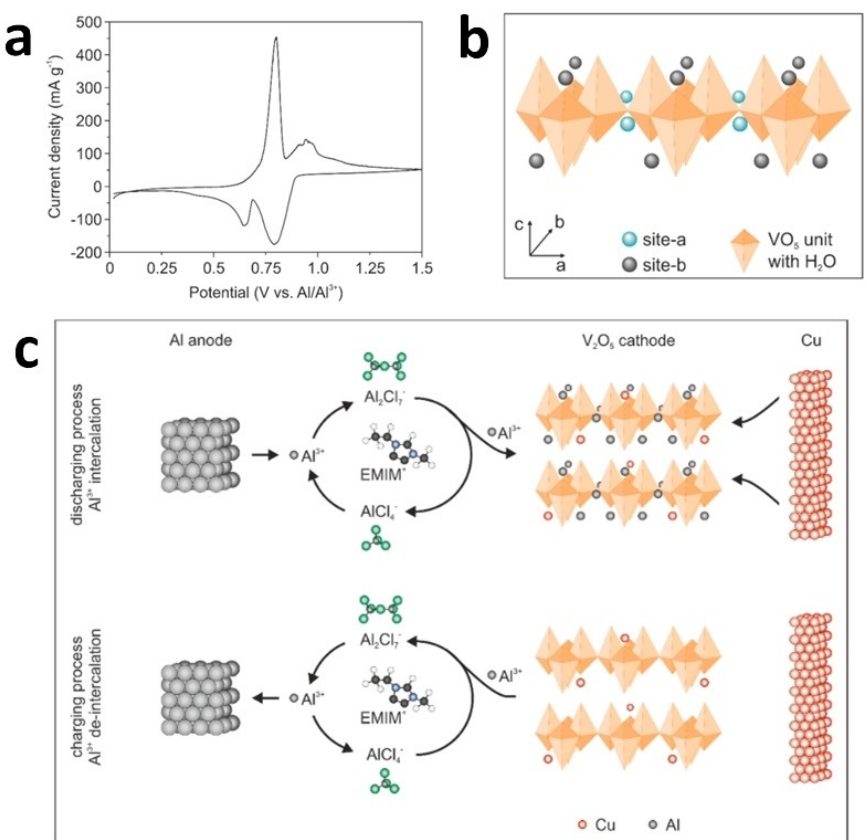


Figure 18. a) Cyclic voltammetry curve of $V_2O_5 \cdot 1.15H_2O$ at a scan rate of 0.1 mVs^{-1} revealing two (de)intercalation potentials. b) Schematic illustration of the two different intercalation sites near the planar oxygen atom (site-a) and close to the apical oxygen atom (site-b). c) Simplified schematic representation of the occurring reactions during the discharge and charge process in the Cu doped V_2O_5 cathode. Reproduced with permission from Ref. [176]. Copyright (2020) MDPI (Basel, Switzerland).

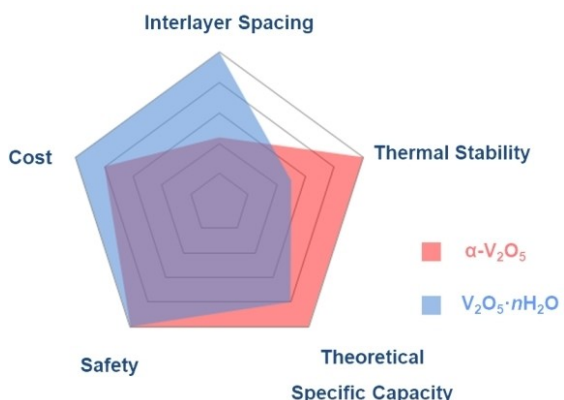


Figure 19. Radar plot comparing the intrinsic characteristics of α -V₂O₅ and V₂O₅·nH₂O as electrode materials for metal-ion batteries.

xerogels and aerogels. It has a large *d*-spacing (such as ~11.5 Å for V₂O₅·H₂O). Due to the large interlayer spacing and the “shielding effect” of water molecules, almost all metal charge carriers, including Li⁺, Na⁺, K⁺, Mg²⁺, Zn²⁺, Ca²⁺, and Al³⁺, could be inserted and extracted smoothly along with the shrinkage and expansion of the interlayer spacings, which generally displays higher specific capacities and faster reaction kinetics compared with α -V₂O₅.

Based on the data reported in the literature, it seems that α -V₂O₅ and V₂O₅·nH₂O exhibit the best compatibility with LIBs and ZIBs, respectively, in terms of reversible capacity and cycling stability. The future research of V₂O₅ as electrode materials for metal-ions batteries should be focused on the following directions:

1. Although α -V₂O₅ has a much higher theoretical specific capacity than LiCoO₂ used in commercial LIBs. Compared with LiCoO₂, it suffers from a lower working voltage and multiple voltage plateaus which are unfavorable for practical applications. In this regard, ions doping may be helpful to enhance the working voltage and/or further increase the specific capacity of α -V₂O₅.
2. Except for LIBs, the reaction kinetics of α -V₂O₅ is poor in other metal-ion batteries due to the large size of Na-and K-ions and the multivalent nature of Mg-, Zn-, Ca-, and Al-ions. Expanding the interlayer spacings by introducing water molecules to form V₂O₅·nH₂O is a simple and effective approach to enhance kinetics. The correlation between water number *n* in V₂O₅·nH₂O and electrochemical performance, such as specific capacities, cycling stability, and rate performances of V₂O₅·nH₂O as electrode materials for metal-ion batteries, needs to be studied quantitatively.
3. α -V₂O₅ and V₂O₅·nH₂O are usually studied as cathode materials for metal-ions batteries. However, since they do not contain any metal charge carriers in the pristine states, they cannot be directly used in full-cells in which metal-ions free anodes are used. Thus, to expand the applications of α -V₂O₅ and V₂O₅·nH₂O to pair with nonmetal anode materials, effective chemical or electrochemical metal-ions pre-insertion approaches should be developed in the future.

4. The optimal crystalline structures of V₂O₅ for the insertion-extraction of different charge carriers need to be established by experimental investigations aided by theoretical calculations. These V₂O₅ phases should possess abundant vacant sites to accommodate a large amount of metal charge carriers and exhibit small diffusion barriers for metal charge carriers migration.
5. The structure evolutions of α -V₂O₅ and V₂O₅·nH₂O as electrode materials for metal-ion batteries were usually studied in half cell systems which using metal as counter electrodes. However, for practical applications, these materials usually work as either cathode or anode materials in full cell systems. Thus, the electrochemical reaction mechanism of them in full cell systems need to be studied in the future to assess their real potential for practical applications.
6. States of charge (SoC) is one of the key points for batteries to avoid overcharging and over-discharging. As the multiple oxidation states (ranging from +2 to +5) of vanadium, α -V₂O₅ undergoes a series of reversible phase transitions during lithium insertion-extraction and its charge-discharge curves are stepped. This provides convenience for roughly determining the SoC by its voltage.

In brief, this review comprehensively and comparatively discusses the structure evolution of α -V₂O₅ and V₂O₅·nH₂O during different kinds of metal-ions insertion-extraction. It is expected to be helpful for understanding the interaction between V₂O₅ and different charge carriers and inspire the exploration of other high-performance vanadium-based layered materials for rechargeable batteries.

Acknowledgements

The authors acknowledge the financial support from the National Natural Science Foundation of China (52172177) and the China Postdoctoral Science Foundation (2022M720350).

Conflict of Interests

The authors declare no conflict of interest.

Keywords: electrode materials • metal-ion batteries • structural evolution • V₂O₅

- [1] X. Kuai, K. Li, J. Chen, H. Wang, J. Yao, C. L. Chiang, T. Liu, H. Ye, J. Zhao, Y. G. Lin, L. Zhang, V. Nicolosi, L. Gao, *ACS Nano* **2022**, *16*, 1502.
- [2] O. J. Guerra, J. Eichman, P. Denholm, *Energy Environ. Sci.* **2021**, *14*, 5132.
- [3] M. S. Zantye, A. Arora, M. M. F. Hasan, *Energy Environ. Sci.* **2021**, *14*, 3986.
- [4] S. Yan, K. P. Abhilash, L. Tang, M. Yang, Y. Ma, Q. Xia, Q. Guo, *Small* **2019**, *15*, 1804371.
- [5] Z. Wei, D. Wang, X. Yang, C. Wang, G. Chen, F. Du, *Adv. Mater. Interfaces* **2018**, *5*, 1800639.
- [6] Y. Wen, K. He, Y. Zhu, F. Han, Y. Xu, I. Matsuda, Y. Ishii, J. Cumings, C. Wang, *Nat. Commun.* **2014**, *5*, 4033.
- [7] Z. Li, H. Zhao, *J. Mater. Chem. A* **2018**, *6*, 24013.

- [8] E. J. Kim, P. A. Maughan, E. N. Bassey, R. J. Clément, L. A. Ma, L. C. Duda, D. Sehrawat, R. Younesi, N. Sharma, C. P. Grey, A. R. Armstrong, *Adv. Energy Mater.* **2022**, *12*, 2102325.
- [9] H. Kim, J. C. Kim, S.-H. Bo, T. Shi, D.-H. Kwon, G. Ceder, *Adv. Energy Mater.* **2017**, *7*, 1700098.
- [10] B. Cao, Q. Zhang, H. Liu, B. Xu, S. Zhang, T. Zhou, J. Mao, W. K. Pang, Z. Guo, A. Li, J. Zhou, X. Chen, H. Song, *Adv. Energy Mater.* **2018**, *8*, 1801149.
- [11] D. S. Charles, M. Feygenson, K. Page, J. Neufeld, W. Xu, X. Teng, *Nat. Commun.* **2017**, *8*, 15520.
- [12] J. C. Pramudita, D. Sehrawat, D. Goonetilleke, N. Sharma, *Adv. Energy Mater.* **2017**, *7*, 1602911.
- [13] M. Wang, H. Zhang, J. Cui, S. Yao, X. Shen, T. J. Park, J. K. Kim, *Energy Storage Mater.* **2021**, *39*, 305.
- [14] H. J. Kim, J. H. Jo, J. U. Choi, N. Voronina, D. Ahn, T. Y. Jeon, H. Yashiro, Y. Anisovich, G. Ragoisha, E. Streltsov, S. T. Myung, *Energy Storage Mater.* **2021**, *40*, 197.
- [15] P. R. Kumar, K. Kubota, Y. Miura, M. Ohara, K. Gotoh, S. Komaba, *J. Power Sources* **2021**, *493*, 229676.
- [16] L. Zhou, Q. Liu, Z. Zhang, K. Zhang, F. Xiong, S. Tan, Q. An, Y. M. Kang, Z. Zhou, L. Mai, *Adv. Mater.* **2018**, *30*, 1801984.
- [17] J. Muldoon, C. B. Bucur, A. G. Oliver, T. Sugimoto, M. Matsui, H. S. Kim, G. D. Allred, J. Zajicek, Y. Kotani, *Energy Environ. Sci.* **2012**, *5*, 5941.
- [18] S. Islam, M. H. Alfarouqi, D. Y. Putro, V. Soundharrajan, B. Sambandam, J. Jo, S. Park, S. Lee, V. Mathew, J. Kim, *J. Mater. Chem. A* **2019**, *7*, 20335.
- [19] C. Liu, Z. Neale, J. Zheng, X. Jia, J. Huang, M. Yan, M. Tian, M. Wang, J. Yang, G. Cao, *Energy Environ. Sci.* **2019**, *12*, 2273.
- [20] J. Ding, Z. Du, B. Li, L. Wang, S. Wang, Y. Gong, S. Yang, *Adv. Mater.* **2019**, *31*, 1904369.
- [21] H. Qiu, X. Du, J. Zhao, Y. Wang, J. Ju, Z. Chen, Z. Hu, D. Yan, X. Zhou, G. Cui, *Nat. Commun.* **2019**, *10*, 5374.
- [22] L. Geng, X. Wang, K. Han, P. Hu, L. Zhou, Y. Zhao, W. Luo, L. Mai, *ACS Energy Lett.* **2022**, *7*, 247.
- [23] J. Wang, S. Tan, F. Xiong, R. Yu, P. Wu, L. Cui, Q. An, *Chem. Commun.* **2020**, *56*, 3805.
- [24] Y. Murata, S. Takada, T. Obata, T. Tojo, R. Inada, Y. Sakurai, *Electrochim. Acta* **2019**, *294*, 210.
- [25] Y. Wu, M. Gong, M. C. Lin, C. Yuan, M. Angell, L. Huang, D. Y. Wang, X. Zhang, J. Yang, B. J. Hwang, H. Dai, *Adv. Mater.* **2016**, *28*, 9218.
- [26] C. Wu, S. Gu, Q. Zhang, Y. Bai, M. Li, Y. Yuan, H. Wang, X. Liu, Y. Yuan, N. Zhu, F. Wu, H. Li, L. Gu, J. Lu, *Nat. Commun.* **2019**, *10*, 73.
- [27] S. Liu, J. J. Hu, N. F. Yan, G. L. Pan, G. R. Li, X. P. Gao, *Energy Environ. Sci.* **2012**, *5*, 9743.
- [28] X. Zhang, D. Yu, Z. Wei, N. Chen, G. Chen, Z. X. Shen, F. Du, *ACS Appl. Mater. Interfaces* **2021**, *13*, 18897.
- [29] C. Xia, J. Guo, P. Li, X. Zhang, H. N. Alshareef, *Angew. Chem. Int. Ed.* **2018**, *130*, 4007.
- [30] C. Li, L. Gu, J. Tong, S. Tsukimoto, J. Maier, *Adv. Funct. Mater.* **2011**, *21*, 1391.
- [31] B. He, G. Cheng, S. Zhao, X. Zeng, Y. Li, R. Yang, M. Sun, L. Yu, *J. Solid State Chem.* **2019**, *269*, 305.
- [32] J. Cao, D. Zhang, Y. Yue, T. Pakornchote, T. Bovornratanarak, X. Zhang, Z. Zeng, J. Qin, Y. Huang, *ACS Appl. Mater. Interfaces* **2022**, *14*, 7909.
- [33] Y. Bai, X. Zhou, C. Zhan, L. Ma, Y. Yuan, C. Wu, M. Chen, G. Chen, Q. Ni, F. Wu, R. Shahbazian-Yassar, T. Wu, J. Lu, K. Amine, *Nano Energy* **2017**, *32*, 10.
- [34] Y. Huang, Z. Deng, W. Wang, C. Liang, J. She, S. Deng, N. Xu, *Sci. Rep.* **2015**, *5*, 10631.
- [35] J. Ding, H. Zheng, H. Gao, Q. Liu, Z. Hu, L. Han, S. Wang, S. Wu, S. Fang, S. Chou, *Adv. Energy Mater.* **2021**, *11*, 2100973.
- [36] Q. Yin, J. Luo, J. Zhang, S. Zhang, J. Han, Y. Lin, J. Zhou, L. Zheng, M. Wei, *Adv. Funct. Mater.* **2020**, *30*, 1907448.
- [37] P. He, M. Yan, G. Zhang, R. Sun, L. Chen, Q. An, L. Mai, *Adv. Energy Mater.* **2017**, *7*, 1601920.
- [38] H. Tian, X. Yu, H. Shao, L. Dong, Y. Chen, X. Fang, C. Wang, W. Han, G. Wang, *Adv. Energy Mater.* **2019**, *9*, 1901560.
- [39] S. Wang, S. Zhao, X. Guo, G. Wang, *Adv. Energy Mater.* **2022**, *12*, 2100864.
- [40] A. Khan, J. Azadmanjiri, B. Wu, L. Liping, Z. Sofer, J. Min, *Adv. Energy Mater.* **2021**, *11*, 2100451.
- [41] H. Chen, X. Xiao, Q. Zhu, P. Zhang, X. Wang, B. Xu, *ACS Appl. Mater. Interfaces* **2022**, *14*, 46502.
- [42] M. Kong, K. Liu, J. Ning, J. Zhou, H. Song, *J. Mater. Chem. A* **2017**, *5*, 19280.
- [43] M. Okubo, D. Asakura, Y. Mizuno, J. D. Kim, T. Mizokawa, T. Kudo, I. Honma, *J. Phys. Chem. Lett.* **2010**, *1*, 2063.
- [44] J. H. Lee, G. Ali, D. H. Kim, K. Y. Chung, *Adv. Energy Mater.* **2017**, *7*, 1601491.
- [45] J. Liao, Q. Hu, J. Mu, X. He, S. Wang, C. Chen, *Chem. Commun.* **2019**, *55*, 659.
- [46] D. Ji, H. Zheng, H. Zhang, W. Liu, J. Ding, *Chem. Eng. J.* **2022**, *433*, 133815.
- [47] N. Tolganbek, A. Mentbayeva, N. Serik, N. Batyrgali, M. Naizakarayev, K. Kanamura, Z. Bakenov, *J. Power Sources* **2021**, *493*, 229686.
- [48] C. Zhang, Q. Wang, Y. Song, G. Wang, H. Wang, *Carbon N Y* **2023**, *201*, 76.
- [49] A. J. Naylor, J. M. Garcia-lastra, T. Vegge, F. Klein, P. Norby, K. Edström, M. Hahlin, *J. Mater. Chem. A* **2019**, *2*, 21244.
- [50] A. Sakuda, T. Takeuchi, K. Okamura, H. Kobayashi, H. Sakaebe, K. Tatsumi, Z. Ogumi, *Sci. Rep.* **2014**, *4*, 4883.
- [51] Q. Wang, A. Sarkar, D. Wang, L. Velasco, R. Azmi, S. S. Bhattacharya, T. Bergfeldt, A. Düvel, P. Heitjans, T. Brezesinski, H. Hahn, B. Breitung, *Energy Environ. Sci.* **2019**, *12*, 2433.
- [52] H. Kim, D. H. Seo, A. Urban, J. Lee, D. H. Kwon, S. H. Bo, T. Shi, J. K. Papp, B. D. McCloskey, G. Ceder, *Chem. Mater.* **2018**, *30*, 6532.
- [53] H. Huang, D. Li, L. Hou, H. Du, H. Wei, X. Liu, Q. Wang, Y. Wei, *J. Power Sources* **2022**, *542*, 231755.
- [54] B. Huang, L. Cheng, X. Li, Z. Zhao, J. Yang, Y. Li, Y. Pang, G. Cao, *Small* **2022**, *18*, 2107697.
- [55] M. S. Whittingham, *J. Electrochem. Soc.* **1976**, *123*, 315.
- [56] T. M. Gür, *Energy Environ. Sci.* **2018**, *11*, 2696.
- [57] S. Batool, M. Idrees, S. T. Han, Y. Zhou, *Adv. Sci.* **2022**, *10*, 2203956.
- [58] J. H. Jo, J. Y. Hwang, J. U. Choi, H. J. Kim, Y. K. Sun, S. T. Myung, *J. Power Sources* **2019**, *432*, 24.
- [59] Z. Jian, Y. S. Hu, X. Ji, W. Chen, *Adv. Mater.* **2017**, *29*, 1601925.
- [60] A. Moretti, S. Passerini, *Adv. Energy Mater.* **2016**, *6*, 1600868.
- [61] Q. Fu, H. Zhao, A. Sarapulova, S. Dsoke, *Appl. Res.* **2022**, e202200070.
- [62] X. Xu, F. Xiong, J. Meng, X. Wang, C. Niu, Q. An, L. Mai, *Adv. Funct. Mater.* **2020**, *30*, 1904398.
- [63] G. Chen, Q. Huang, T. Wu, L. Lu, *Adv. Funct. Mater.* **2020**, *30*, 2001289.
- [64] X. Wang, Y. Li, S. Wang, F. Zhou, P. Das, C. Sun, S. Zheng, Z. S. Wu, *Adv. Energy Mater.* **2020**, *10*, 2000081.
- [65] K. Yuan, R. Ning, M. Bai, N. Hu, K. Zhang, J. Gu, Q. Li, Y. Huang, C. Shen, K. Xie, *Energy Technol.* **2019**, *8*, 1900796.
- [66] D. Zhao, L. Zheng, Y. Xiao, X. Wang, M. Cao, *ChemSusChem* **2015**, *8*, 2212.
- [67] P. De, J. Halder, S. Priya, A. K. Srivastava, A. Chandra, *ACS Appl. Energ. Mater.* **2023**, *6*, 753.
- [68] H. Wang, Y. I. I. Jang, B. Huang, D. R. Sadoway, Y. M. Chiang, *J. Electrochem. Soc.* **1999**, *146*, 473.
- [69] F. Lanlan, L. Zhenhuan, D. Nanping, *Energy Storage Mater.* **2021**, *41*, 152.
- [70] J. Yao, Y. Li, R. C. Massé, E. Uchaker, G. Cao, *Energy Storage Mater.* **2018**, *11*, 205.
- [71] S. K. Park, W. M. Dose, B. D. Boruah, M. De Volder, *Adv. Mater. Technol.* **2022**, *7*, 2100799.
- [72] Y. Li, J. Yao, E. Uchaker, J. Yang, Y. Huang, M. Zhang, G. Cao, *Adv. Energy Mater.* **2013**, *3*, 1171.
- [73] V. Petkov, P. N. Trikalitis, E. S. Bozin, S. J. L. Billinge, T. Vogt, M. G. Kanatzidis, *J. Am. Chem. Soc.* **2002**, *124*, 10157.
- [74] M. Giorgetti, S. Passerini, W. H. Smyrl, M. Berrettoni, *Inorg. Chem.* **2000**, *39*, 1514.
- [75] H. H. Kristoffersen, H. Metiu, *J. Phys. Chem. C* **2016**, *120*, 3986.
- [76] M. G. Kanatzidis, C.-G. Wu, Y.-J. Liu, D. C. DeGroot, J. L. Schindler, H. O. Marcy, C. R. Kannewurf, *J. Electrochem. Soc.* **2004**, *151*, A1.
- [77] M. Giorgetti, M. Berrettoni, S. Passerini, W. H. Smyrl, *Electrochim. Acta* **2002**, *47*, 3163.
- [78] F. Coustier, S. Passerini, W. H. Smyrl, *Electrochim. Soc. Lett.* **1998**, *145*, 73.
- [79] D. B. Le, S. Passerini, F. Coustier, J. Guo, T. Soderstrom, B. B. Owens, W. H. Smyrl, *Chem. Mater.* **1998**, *10*, 682.
- [80] V. V. Porsev, A. V. Bandura, R. A. eVarestov, *Surf. Sci.* **2017**, *666*, 76.
- [81] H. E. M. Hussein, R. Beanland, A. M. Sánchez, D. Walker, M. Walker, Y. Han, J. V. Macpherson, *J. Mater. Chem. A* **2022**, *10*, 8515.
- [82] C. Delmas, H. Cognac-Auradou, J. M. Cocciantelli, M. Ménétrier, J. P. Doumerc, *Solid State Ionics* **1994**, *69*, 257.
- [83] G. A. Horrocks, M. F. Likely, J. M. Velazquez, S. Banerjee, *J. Mater. Chem. A* **2013**, *1*, 15265.

- [84] S. Ki Park, P. Nakhanivej, J. Seok Yeon, K. Ho Shin, W. M. Dose, M. De Volder, J. Bae Lee, H. Jin Kim, H. S. Park, *J. Energy Chem.* **2021**, *55*, 108.
- [85] L. R. De Jesus, J. L. Andrews, A. Parija, S. Banerjee, *ACS Energy Lett.* **2018**, *3*, 915.
- [86] J. M. Cocciantelli, J. P. Doumerc, M. Pouchard, M. Broussely, J. Labat, *J. Power Sources* **1991**, *34*, 103.
- [87] R. J. Cava, A. Santoro, D. W. Murphy, S. M. Zahirak, R. M. Fleming, P. Marsh, R. S. Roth, *J. Solid State Chem.* **1986**, *65*, 63.
- [88] Z. Wang, S. Yuan, X. Tang, H. Wang, M. Zhang, F. Liu, N. Yao, Y. Ma, *Energy Storage Mater.* **2023**, *54*, 284.
- [89] B. Z. Yang, P. Xie, Q. Luo, Z. W. Li, C. Y. Zhou, Y. H. Yin, X. Bin Liu, Y. S. Li, Z. P. Wu, *Adv. Funct. Mater.* **2022**, *32*, 2110665.
- [90] X. Lan, L. Wang, L. Yu, Y. Li, X. Hu, *ACS Materials Lett.* **2021**, *3*, 1394.
- [91] C. K. Christensen, D. R. Sørensen, J. Hvam, D. B. Ravnsbæk, *Chem. Mater.* **2019**, *31*, 512.
- [92] A. Mukherjee, H. A. Ardakanian, T. Yi, J. Cabana, R. Shahbazian-Yassar, R. F. Klie, *Appl. Phys. Lett.* **2017**, *110*, 213903.
- [93] J. Zhu, H. Shen, X. Shi, F. Yang, X. Hu, W. Zhou, H. Yang, M. Gu, *Anal. Chem.* **2019**, *91*, 11055.
- [94] S. Osman, C. Peng, J. Shen, F. Li, W. Huang, J. Liu, J. Liu, D. Xue, M. Zhu, *Nano Energy* **2022**, *100*, 107481.
- [95] S. Tian, T. Cai, D. Wang, D. Kong, H. Ren, W. Xing, *IOP Conf. Ser. Earth Environ. Sci.* **2021**, *692*, 022042.
- [96] G. Ali, J. H. Lee, S. H. Oh, B. W. Cho, K. W. Nam, K. Y. Chung, *ACS Appl. Mater. Interfaces* **2016**, *8*, 6032.
- [97] G. Zhang, Y. Zhang, S. Bao, L. Zhang, *Minerals* **2019**, *9*, 271.
- [98] M. S. Renard, N. Emery, R. Baddour-Hadjean, J. P. Pereira-Ramos, *Electrochim. Acta* **2017**, *252*, 4.
- [99] M. Safrany Renard, N. Emery, E. M. Roginskii, R. Baddour-Hadjean, J. P. Pereira-Ramos, *J. Solid State Chem.* **2017**, *254*, 62.
- [100] R. Baddour-Hadjean, A. Marzouk, J. P. Pereira-Ramos, *J. Raman Spectrosc.* **2012**, *43*, 153.
- [101] N. Emery, R. Baddour-Hadjean, D. Batyrbekuly, B. Laik, Z. Bakenov, J.-P. Pereira-Ramos, *Chem. Mater.* **2018**, *5*, 5305.
- [102] J. Hao, H. Xia, A. M. Rao, Y. He, J. Zhou, B. Lu, *Energy Storage Mater.* **2022**, *53*, 148.
- [103] F. Ye, D. Lu, X. Gui, T. Wang, X. Zhuang, W. Luo, Y. Huang, *J. Mater.* **2019**, *5*, 344.
- [104] G. Liang, Z. Gan, X. Wang, X. Jin, B. Xiong, X. Zhang, S. Chen, Y. Wang, H. He, C. Zhi, *ACS Nano* **2021**, *15*, 17717.
- [105] L. Deng, X. Niu, G. Ma, Z. Yang, L. Zeng, Y. Zhu, L. Guo, *Adv. Funct. Mater.* **2018**, *28*, 1800670.
- [106] Y. Zhang, X. Niu, L. Tan, L. Deng, S. Jin, L. Zeng, H. Xu, Y. Zhu, *ACS Appl. Mater. Interfaces* **2020**, *12*, 93320.
- [107] B. Zhou, H. Shi, R. Cao, X. Zhang, Z. Jiang, *Phys. Chem. Chem. Phys.* **2014**, *16*, 18578.
- [108] A. Mukherjee, N. Sa, P. J. Phillips, A. Burrell, J. Vaughney, R. F. Klle, *Chem. Mater.* **2017**, *29*, 2218.
- [109] G. Sai Gautam, P. Canepa, A. Abdellahi, A. Urban, R. Malik, G. Ceder, *Chem. Mater.* **2015**, *27*, 3733.
- [110] H. D. Yoo, J. R. Jokisaari, Y. S. Yu, B. J. Kwon, L. Hu, S. Kim, S. D. Han, M. Lopez, S. H. Lapidus, G. M. Nolis, B. J. Ingram, I. Bolotin, S. Ahmed, R. F. Klle, J. T. Vaughney, T. T. Fister, J. Cabana, *ACS Energy Lett.* **2019**, *4*, 1528.
- [111] H. Search, C. Journals, A. Contact, M. lopscience, *J. Phys. Condens. Matter.* **1998**, *10*, 1229.
- [112] M. Konstantinović, Z. Popović, *Phys. Rev. B* **2000**, *61*, 15185.
- [113] J. Yang, X. Wang, J. Wang, X. Dong, L. Zhu, D. Hou, W. Zeng, J. Wang, F. Pan, *Appl. Surf. Sci.* **2021**, *569*, 150983.
- [114] G. Gershinsky, H. D. Yoo, Y. Gofer, D. Aurbach, *Langmuir* **2013**, *29*, 10964.
- [115] V. P. Filonenko, M. Sundberg, P. E. Werner, I. P. Zibrov, *Acta Crystallogr. Sect. B* **2004**, *60*, 375.
- [116] A. Sarkar, S. Sau, D. Muthuraj, S. Mitra, *J. Power Sources* **2022**, *541*, 231669.
- [117] T. K. Thuan Ngoc Vo, Hyeongwoo Kim, Jaehyun Hur, Wonchang Choi, *J. Mater. Chem. A* **2018**, *8*, 22645.
- [118] M. R. P. Rafael Trócoli, Prakash Parajuli, Carlos Frontera, Ashley P. Black, Grant C. B. Alexander, Indrani Roy, M. Elena Arroyo-de Domípablo, Robert F. Klle, Jordi Cabana, *ACS Appl. Energ. Mater.* **2022**, *5*, 11964–11969.
- [119] J. L. Andrews, A. Mukherjee, H. D. Yoo, A. Parija, P. M. Marley, S. Fakra, D. Prendergast, J. Cabana, R. F. Klle, S. Banerjee, *Chem* **2018**, *4*, 564.
- [120] J. Li, Q. Lin, Z. Zheng, L. Cao, W. Lv, Y. Chen, *ACS Appl. Mater. Interfaces* **2022**, *14*, 12323.
- [121] B. Wu, B. Guo, Y. Chen, Y. Mu, H. Qu, M. Lin, J. Bai, T. Zhao, L. Zeng, *Energy Storage Mater.* **2023**, *54*, 75.
- [122] X. C. Cong Huang, Xin Zhao, Yisu Hao, Yujie Yang, Yang Qian, Ge Chang, Yan Zhang, Qunli Tang, Aiping Hu, *Small* **2022**, *18*, 2203674.
- [123] Y. Zhang, S. Jiang, Y. Li, X. Ren, P. Zhang, L. Sun, H. Y. Yang, *Adv. Energy Mater.* **2023**, *13*, 2202826.
- [124] X. Chen, L. Wang, H. Li, F. Cheng, J. Chen, *J. Energy Chem.* **2019**, *38*, 20.
- [125] Y. Lu, T. Zhu, W. Bergh, M. Stefk, K. Huang, *Angew. Chem.* **2020**, *132*, 17152.
- [126] N. Zhang, Y. Dong, M. Jia, X. Bian, Y. Wang, M. Qiu, J. Xu, Y. Liu, L. Jiao, F. Cheng, *ACS Energy Lett.* **2018**, *3*, 1366.
- [127] H. Liu, L. Jiang, B. Cao, H. Du, H. Lu, Y. Ma, H. Wang, H. Guo, Q. Huang, B. Xu, S. Guo, *ACS Nano* **2022**, *16*, 14539.
- [128] P. Byeon, Y. Hong, H. Bin Bae, J. Shin, J. W. Choi, S. Y. Chung, *Nat. Commun.* **2021**, *12*, 4599.
- [129] Y. Lu, T. Zhu, W. van den Bergh, M. Stefk, K. Huang, *Angew. Chem. Int. Ed.* **2020**, *59*, 17004.
- [130] Z. Yao, Q. Wu, K. Chen, J. Liu, C. Li, *Energy Environ. Sci.* **2020**, *13*, 3149.
- [131] G. S. Gautam, P. Canepa, R. Malik, M. Liu, K. Persson, G. Ceder, *Chem. Commun.* **2015**, *51*, 13619.
- [132] Y. S. Yoshiaki Murata, Z. Ryoji Inada, *J. Electrochem. Soc.* **2021**, *168*, 020528.
- [133] M. E. Purbarani, J. Hyoung, S. Hong, *ACS Appl. Energ. Mater.* **2021**, *4*, 7487.
- [134] D. Wang, H. Liu, J. D. Elliott, L. M. Liu, W. M. Lau, *J. Mater. Chem. A* **2016**, *4*, 12516.
- [135] A. Parija, D. Prendergast, S. Banerjee, *ACS Appl. Mater. Interfaces* **2017**, *9*, 23756.
- [136] M. C. Lin, M. Gong, B. Lu, Y. Wu, D. Y. Wang, M. Guan, M. Angell, C. Chen, J. Yang, B. J. Hwang, H. Dai, *Nature* **2015**, *520*, 325.
- [137] D. Pal, S. Chakraborty, S. Chattopadhyay, *Energy Technol.* **2021**, *9*, 2100382.
- [138] L. D. Reed, E. Menke, *J. Electrochem. Soc.* **2013**, *160*, 915.
- [139] H. Wang, Y. Bai, S. Chen, X. Luo, C. Wu, F. Wu, J. Lu, K. Amine, *ACS Appl. Mater. Interfaces* **2015**, *7*, 80.
- [140] S. Gu, H. Wang, C. Wu, Y. Bai, H. Li, F. Wu, *Energy Storage Mater.* **2017**, *6*, 9.
- [141] N. Jayaprakash, S. K. Das, L. A. Archer, *Chem. Commun.* **2011**, *47*, 12610.
- [142] T. Das, S. Tosoni, G. Pacchioni, *Comput. Mater. Sci.* **2021**, *191*, 110324.
- [143] A. R. Anggraini, J. Oliver, *Solid State Ionics* **1983**, *9*, 439.
- [144] R. Baddour, J. P. Pereira-Ramos, R. Messina, J. Perichon, *J. Electroanal. Chem.* **1991**, *23*, 81.
- [145] M. Sathiya, A. S. Prakash, K. Ramesha, J. M. Tarascon, A. K. Shukla, *J. Am. Chem. Soc.* **2011**, *133*, 16291.
- [146] S. Passerini, D. B. Le, W. H. Smyrl, M. Berrettoni, R. Tossici, R. Marassi, M. Giorgetti, *Solid State Ionics* **1997**, *104*, 195.
- [147] S. Passerini, W. H. Smyrl, M. Berrettoni, R. Tossici, M. Rosolen, R. Marassi, F. Decker, *Solid State Ionics* **1996**, *90*, 5.
- [148] L. W. Wangoh, Y. Huang, R. L. Jezorek, A. B. Kehoe, G. W. Watson, F. Omenya, N. F. Quackenbush, N. A. Chernova, M. S. Whittingham, L. F. J. Piper, *ACS Appl. Mater. Interfaces* **2016**, *8*, 11532.
- [149] S. Tepavcevic, H. Xiong, V. R. Stamenovic, X. Zuo, M. Balasubramanian, V. B. Prakapenka, C. S. Johnson, T. Rajh, *ACS Nano* **2012**, *6*, 530.
- [150] Q. Liu, Z. F. Li, Y. Liu, H. Zhang, Y. Ren, C. J. Sun, W. Lu, Y. Zhou, L. Stanciu, E. A. Stach, J. Xie, *Nat. Commun.* **2015**, *6*, 6127.
- [151] K. H. Xiao, K. M. De, B. L. Jian, L. X. Sheng, Y. L. Jiang, T. Q. Yi, *Chem. Lett.* **2007**, *36*, 560.
- [152] M. Clites, B. W. Byles, E. Pomerantseva, *J. Mater. Chem. A* **2016**, *4*, 7754.
- [153] R. Tang, K. Li, C. Liu, Y. Liu, Y. Gong, J. Lin, *Chem. Eng. J.* **2023**, *453*, 139734.
- [154] M. Tian, C. Liu, J. Zheng, X. Jia, E. P. Jahrman, G. T. Seidler, D. Long, M. Atif, M. Alsalhi, G. Cao, *Energy Storage Mater.* **2020**, *29*, 9.
- [155] D. S. Charles, F. Guo, X. Shan, S. W. Kim, Z. W. Lebens-Higgins, W. Xu, D. Su, L. F. J. Piper, X. Teng, *J. Mater. Chem. A* **2021**, *9*, 15629.
- [156] D. S. Charles, M. Feygenson, K. Page, J. Neufeind, W. Xu, X. Teng, *Nat. Commun.* **2017**, *8*, 15520.
- [157] M. Clites, J. L. Hart, M. L. Taheri, E. Pomerantseva, *ACS Energy Lett.* **2018**, *3*, 562.
- [158] X. Niu, J. Qu, Y. Hong, L. Deng, R. Wang, M. Feng, J. Wang, L. Zeng, Q. Zhang, L. Guo, Y. Zhu, *J. Mater. Chem. A* **2021**, *9*, 13125.
- [159] N. Sa, T. L. Kinnibrugh, H. Wang, G. Sai Gautam, K. W. Chapman, J. T. Vaughney, B. Key, T. T. Fister, J. W. Freeland, D. L. Proffit, P. J. Chupas, G. Ceder, J. G. Barenco, I. D. Bloom, A. K. Burrell, *Chem. Mater.* **2016**, *28*, 2962.

- [160] Q. Fu, X. Wu, X. Luo, S. Indris, A. Sarapulova, M. Bauer, Z. Wang, M. Knapp, H. Ehrenberg, Y. Wei, S. Dsoke, *Adv. Funct. Mater.* **2022**, *32*, 2110674.
- [161] G. Sai Gautam, P. Canepa, W. D. Richards, R. Malik, G. Ceder, *Nano Lett.* **2016**, *16*, 2426.
- [162] Y. Xu, X. Deng, Q. Li, G. Zhang, F. Xiong, S. Tan, Q. Wei, J. Lu, J. Li, Q. An, L. Mai, *Chem* **2019**, *5*, 1194.
- [163] J. Li, Y. Li, J. Yao, B. Huang, J. Jiang, J. Yang, *J. Ind. Eng. Chem.* **2022**, *115*, 554.
- [164] M. Yan, P. He, Y. Chen, S. Wang, Q. Wei, K. Zhao, X. Xu, Q. An, Y. Shuang, Y. Shao, K. T. Mueller, L. Mai, J. Liu, J. Yang, *Adv. Mater.* **2018**, *30*, 1703725.
- [165] Y. Zhang, J. Qin, M. Batmunkh, W. Li, H. Fu, L. Wang, M. Al-Mamun, D. Qi, P. Liu, S. Zhang, Y. L. Zhong, *Small* **2022**, *18*, 2105761.
- [166] J. Sun, Y. Zhao, Y. Liu, H. Jiang, C. Huang, M. Cui, T. Hu, C. Meng, Y. Zhang, *Small Struct.* **2022**, *3*, 2100212.
- [167] T. Wu, K. Zhu, C. Qin, K. Huang, *J. Mater. Chem. A* **2019**, *7*, 5612.
- [168] Z. Feng, Y. Zhang, Y. Zhao, J. Sun, Y. Liu, H. Jiang, M. Cui, T. Hu, C. Meng, *Nanoscale* **2022**, *14*, 8776.
- [169] S. W. Feng Zhang, Xiucui Sun, Min Du, Xiaofei Zhang, Wentao Dong, Yuanhua Sang, Jianjun Wang, Yanlu Li, Hong Liu, *Energy Environ. Mater.* **2021**, *4*, 620.
- [170] D. Kundu, B. D. Adams, V. Duffort, S. H. Vajargah, L. F. Nazar, *Nat. Energy* **2016**, *1*, 16119.
- [171] T. He, Y. Ye, H. Li, S. Weng, Q. Zhang, M. Li, T. Liu, J. Cheng, X. Wang, J. Lu, B. Wang, *Mater. Today* **2021**, *43*, 53.
- [172] S.-T. H. Munseok, S. Chae, Jongwook W. Heo, Jooeun Hyoung, *ChemNanoMat* **2020**, *6*, 1049.
- [173] X. Xu, M. Duan, Y. Yue, Q. Li, X. Zhang, L. Wu, P. Wu, B. Song, L. Mai, *ACS Energy Lett.* **2019**, *4*, 1328.
- [174] B. Jeon, H. H. Kwak, S. T. Hong, *Chem. Mater.* **2022**, *34*, 1491.
- [175] D. B. Le, S. Passerini, F. Coustier, J. Guo, T. Soderstrom, B. B. Owens, W. H. Smyrl, *Chem. Mater.* **1998**, *10*, 682.
- [176] A. M. Diem, B. Fenk, J. Bill, Z. Burghard, *Nanomaterials* **2020**, *10*, 247.
- [177] A. M. Diem, J. Bill, Z. Burghard, *ACS Appl. Energ. Mater.* **2020**, *3*, 4033–4042.
- [178] Q. Fu, A. Sarapulova, L. Zhu, G. Melinte, A. Missyul, E. Welter, X. Luo, M. Knapp, H. Ehrenberg, S. Dsoke, *J. Energy Chem.* **2021**, *62*, 627.
- [179] Y. H. Zhu, Q. Zhang, X. Yang, E. Y. Zhao, T. Sun, X. B. Zhang, S. Wang, X. Q. Yu, J. M. Yan, Q. Jiang, *Chem* **2019**, *5*, 168.
- [180] R. Verrelli, A. P. Black, C. Pattanathummasid, D. S. Tchitchevka, A. Ponrouch, J. Oró-Solé, C. Frontera, F. Bardé, P. Rozier, M. R. Palacín, *J. Power Sources* **2018**, *407*, 162.
- [181] B. Tian, W. Tang, C. Su, Y. Li, *ACS Appl. Mater. Interfaces* **2018**, *10*, 642.

Manuscript received: June 5, 2023

Revised manuscript received: July 7, 2023

Accepted manuscript online: July 9, 2023

Version of record online: July 25, 2023